Mechanical Systems and Signal Processing 235 (2025) 112916

Contents lists available at ScienceDirect

Mechanical Systems and Signal Processing

journal homepage: www.elsevier.com/locate/ymssp

Full Length Article

# Equivalent circuit modeling for triboelectric energy harvesters

Zicheng Liu [a], Guobiao Hu [a,b], Xin Li [a,c], Chaoyang Zhao [a], Yaowen Yang [a,*]

[a] School of Civil and Environmental Engineering, Nanyang Technological University, 50 Nanyang Avenue, 639798, Singapore
[b] The Hong Kong University of Science and Technology (Guangzhou), China
[c] Guangzhou Institute of Technology, Xidian University, China

ARTICLE INFO

Communicated by Daniil Yurchenko

*Keywords:*
Equivalent circuit model
Electromechanical model
Triboelectric energy harvester
Vibration energy harvesting
Internet of Things

ABSTRACT

The utilization of triboelectric transduction for vibration energy harvesting has garnered considerable attention owing to its manifold advantages. Researchers across diverse disciplines have endeavored to develop various theoretical models to investigate the properties of triboelectric energy harvesters (TEHs). Initially, material scientists formulated analytical models to explain triboelectric transduction's electric energy generation process. Subsequently, experts in mechanical engineering devised dynamical models to describe the mechanical response of TEHs, often simplifying the energy extraction circuit (EEC) to a mere resistor. Conversely, researchers in electrical engineering derived models for intricate EECs but tended to oversimplify the harvesters' mechanical response as sinusoidal motions. Consequently, the integration of models addressing both the electromechanical response of the harvesters and the practical EECs remains largely unaddressed due to the analytical challenges posed by such intricate systems. This article presents a novel technique to reconcile the disparity between the electromechanical and EEC models of TEHs by implementing an equivalent circuit model (ECM). Initially, the equivalent circuit parameters of the harvester are identified based on an electromechanical model of a cantilever-based harvester. Subsequently, an ECM encompassing both the mechanical and electrical responses is established. Finally, the ECM is experimentally validated, demonstrating its capability to simulate the harvester's performance on a holistic system level. This proposed methodology serves as a crucial step towards comprehensive modeling and optimization of TEH systems for enhanced energy harvesting efficiency and applicability in various domains.

## 1. Introduction

The maturing concept of the Internet of Things (IoT) has facilitated the widespread deployment of electronic sensors and wearable devices operating within the micro to milli-watt scale. With the rapid spread of such small-scale electronics, a pressing need arises for innovative self-powering solutions. Continuously replacing external power sources, such as batteries—currently the primary power supply for small IoT electronics—becomes impractical. Conversely, ambient vibration emerges as an enticing renewable energy source for low-power IoT devices. Researchers have identified various mechanisms for converting mechanical energy from vibration into electrical energy [1], including piezoelectric [2,3], electromagnetic [4,5], electrostatic [6–8], and triboelectric transductions [9,10]. Among these, triboelectric transduction has gained prominence as a relatively recent approach to developing vibration energy harvesters, offering distinct advantages over its counterparts. Consequently, triboelectric energy harvesters (TEHs) have garnered

* Corresponding author.
*E-mail address:* cywyang@ntu.edu.sg (Y. Yang).

https://doi.org/10.1016/j.ymssp.2025.112916
Received 19 February 2025; Received in revised form 26 April 2025; Accepted 25 May 2025
Available online 2 June 2025

increasing attention due to their high energy-conversion efficiency [11,12], remarkable design flexibility [13,14], cost-effectiveness, and the wide availability of suitable materials.

The development of theoretical models plays a crucial role in designing TEHs to accurately predict their performance, thereby aiding in optimizing their efficiency. Since the pioneering work of Wang *et al.* [15] introducing triboelectric transduction in kinetic energy harvester design, numerous analytical models have emerged [14,16]. While an electrical model elucidating the physics of triboelectric transduction [17] exists, simulating the intricate power generation process of a tribo-pair using such a detailed physical model rooted in fundamental principles like contact electrification and electrostatic induction proves impractical. Consequently, Niu and Wang [18] devised a simplified lumped-parameter equivalent circuit model (ECM) to describe the electrical power generation process involving a tribo-pair. This model treats the tribo-pair as a variable capacitor and an open-circuit voltage source connected in series. Additionally, distinct electrical models have been developed to accommodate different working modes of TEHs, including the contact-separation mode (CS mode) [19], lateral sliding mode [20], freestanding mode [21], and single-electrode mode [22]. For instance, Niu *et al.* established an analytical model for CS-mode TEHs, characterizing their power generation process [19] by relating real-time output voltage ($V$), transferred charge ($Q$), and separation distance ($x$), thus capturing the $V$-$Q$-$x$ behavior of TEHs. Renowned for its adaptability in driving cyclic contact and separation motions through vibration, the CS mode finds extensive application in TEH designs [23,24], making it the basis for the TEH employed in the modeling and experimental work described in this article.

In addition to developing models that address the electrical power generation from triboelectric materials in TEHs, it is essential to establish theoretical models that predict the structural dynamics of TEHs. TEHs comprise supporting structures that drive cyclic relative motions between the materials [23,24]. When coupled with the previously mentioned electrical models, these mechanical models collectively form comprehensive electromechanical models, enabling accurate predictions of TEH performance. In the literature, Fu *et al.* [25] established a lumped-parameter mechanical model for a freestanding TEH based on a three-degree-of-freedom (3DOF) oscillator, coupled with an electrical model specific to freestanding TEHs. Numerical simulations reveal various electromechanical parameters influencing the performance of oscillator-based TEHs. Similarly, Zhao *et al.* derived a lumped-parameter mechanical model tailored for a cantilever-beam-based CS-mode TEH [26], validated through both numerical simulation and experimentation. In a subsequent work by Fu *et al.* [27], the 3DOF oscillator-based TEH was improved by substituting springs with three cantilever beams. Recognizing the limitations of a lumped-parameter model in simulating the vibration response of three interacting beam structures, they developed a distributed-parameter model to facilitate numerical simulation of the TEH's electromechanical response. With available mechanical models for oscillator-based TEHs under general vibration conditions, electromechanical models for TEHs subjected to vibrations induced by various external sources can be established. For instance, Zhao *et al.* developed a distributed-parameter model for a cantilever-beam-based TEH with a bluff body subjected to aerodynamic force due to the fluid–structure interaction phenomenon [24]. This model, validated through numerical simulations and experiments, reveals critical parameters impacting TEH performance under wind-induced vibrations.

In addition to the mechanical structure and electrical component, the EEC represents another pivotal component in a triboelectric energy harvesting system. However, existing studies on the electromechanical models of TEHs, including those mentioned previously, often oversimplify the EEC into a single resistor. Yet, solely using a resistor to represent the EEC proves impractical due to the pulsed nature of TEH output signals and the substantial impedance mismatch between TEHs and conventional energy storage units like capacitors and batteries [17]. Therefore, it is necessary to develop corresponding models for EECs to aid the system-level optimization study of power management circuits for TEHs. Pioneering this endeavor, Pathak and Kumar have developed the theoretical models for several nonlinear EECs specific to TEHs [28]. The analytical models for the full-wave-rectifier circuit (FWRC), the parallel synchronized switch harvesting on inductor (P-SSHI), the series synchronized switch harvesting on inductor (S-SSHI), and the synchronized charge extraction (SCE) circuits were derived, and the power extraction efficacies of these circuits are evaluated and compared. More detailed models for the P-SSHI and the S-SSHI applied on TEHs were also developed and validated through experiments [29]. Their work has demonstrated that the P-SSHI and S-SSHI circuits exhibit superior power-extraction efficiency compared to the FWRC. They have also developed and experimentally validated an analytical model for a pre-biased SCE, illustrating how pre-biasing can boost the power extraction efficiency compared to a standard SCE circuit [30,31]. Nevertheless, it is essential to note that these studies simplified the mechanical responses of the TEHs as purely sinusoidal, overlooking factors that genuinely influence the TEH's mechanical behavior, such as impact and electrostatic forces. In reality, the contact-separation cycles involve these complex factors, rendering the mechanical response of a practical TEH far from being simply sinusoidal motions. Consequently, there is a pressing need to develop a comprehensive model capable of amalgamating the electromechanical characteristics of TEHs with their corresponding circuit models, ensuring a more accurate representation of their real-world behavior.

The preceding paragraph has pointed out a considerable disparity between the electromechanical and EEC models of TEHs. This article endeavors to reconcile this division by proposing an ECM tailored for TEHs, enabling comprehensive system-level simulations for precise performance prediction. An ECM, fundamentally, is a simulation model that characterizes the operations of an electromechanical system using electrical circuit components to represent its parameters and variables [32]. Following pioneering work by Elvin and Elvin [33] and Yang and Tang [34] in establishing and validating an ECM for general piezoelectric energy harvesting systems, ECMs have become a staple tool for researchers exploring various piezoelectric energy harvester (PEH) designs incorporating nonlinear EECs. For instance, Zhao *et al.* [35] developed an ECM for a galloping PEH, demonstrating its efficacy through experimental validation when subjected to an SCE circuit. Similarly, Jia et al. [36] constructed and experimentally validated an ECM for a vortex-induced PEH, employing it for a parametric investigation of the harvester. Another notable example is the work of Bayik et al. [37], who devised an ECM for a thin-plate piezoelectric energy harvesting system with various EEC configurations.

In contrast with the wide application of ECMs for system-level simulations in piezoelectric energy harvesting, integrating the electromechanical models of TEHs with the EEC models into comprehensive system-level simulations has remained an unchartered

territory. The reason is that the electromechanical and practical EEC models of TEHs are both highly nonlinear [25,28], which deters researchers from different disciplines from developing system-level analytical models as they have different foci of study. This situation is entirely different from piezoelectric energy harvesting systems because the electromechanical model of the piezoelectric harvester itself can be completely linear [34]. Furthermore, even if a system-level analytical model of a TEH with an EEC is developed, it is still cumbersome to translate it into computer-readable code and look for a suitable numerical solver for simulation. So far, the simulation of the electromechanical models of TEHs has relied on programming environments such as MATLAB [26,38] by translating the governing equations into computer-readable code. In contrast, electrical energy extraction and management circuit simulations have typically been conducted using circuit simulation software like Simetrix and PSpice [29,30]. By introducing the ECM, this article addresses such a disparity. It will demonstrate that holistic system-level simulations of the operational characteristics of TEHs with EECs applied can be accomplished in circuit simulation software tools like PSpice, Simetrix, Simscape, and Simulink. If the nonlinear electromechanical models of TEHs are translated into equivalent pseudo-circuit components and incorporated into circuit simulation software, system-level simulations can be achieved along with the EEC models. These simulations rely on mechanical parameters of the TEH determined through its analytical model's analogy to the circuit counterpart, which is subsequently converted into ECM parameters. Furthermore, the proposed ECM also preserves the nonlinearity and back-and-forth coupling of the electromechanical model through innovative circuitry manipulations. The ECM serves as a reliable tool for future optimizations of TEH systems, especially when more intricate nonlinear electromechanical or EEC models are involved, similar to how ECMs have been used for such purposes in PEH systems [39,40].

Briefly speaking, compared to prior studies that either oversimplified the mechanical model or neglected realistic circuit interactions, the proposed ECM captures both domains in a unified, bidirectionally coupled framework. Table 1 summarizes the key differences between this study and representative prior modeling efforts. However it is noteworthy that the primary contribution of this work lies not in improving computational efficiency, but in enabling accurate system-level simulations of TEHs within a circuit simulation environment, particularly when coupling the electromechanical model with nonlinear EECs. This level of integration was previously not feasible using conventional ODE-based methods alone.

The proposed ECM framework reformulates the electromechanical dynamics, including nonlinear contact interactions, into a structure compatible with standard circuit simulation tools such as SPICE, Simscape, and Simetrix. This compatibility allows the mechanical and electrical subsystems to be simulated concurrently, supporting seamless co-design, rapid prototyping, and realistic performance evaluation of complete TEH systems.

The rest of this article starts with illustrating the design and mechanism of the TEH employed for simulation and experimental validation in this study. Subsequently, the electrical and circuit equivalence of the mechanical parameters utilized in the ECM is determined through an analysis of the theoretical model of the TEH. In addition to parameter identification, this study introduces an innovative element: a pseudo-capacitor that serves as a mathematical component, effectively coupling the circuit equivalent of the TEH's electromechanical model. Following the development of the ECM, its simulation results are validated against experimental data obtained using identical parameters. Lastly, the versatility of the ECM is demonstrated through its capability to simulate the TEH's response when connected to a practical nonlinear EEC, validated by a series of experiments. The comprehensive equivalent circuit modeling approach provides a valuable tool for comprehending and optimizing the performance of TEHs in practical applications.

## 2. Structural design of TEH

Fig. 1 (a) illustrates the structure of the TEH employed in this study. A cantilever structure is chosen for ease of fabrication, maintaining generalizability to other CS-mode TEHs. The distributed-parameter model later introduced for such a structure can be converted into a lumped-parameter model equivalent to a spring-mass-damper system, applicable to numerous parallel-plate CS-mode TEHs. The left end of the cantilever beam, serving as the supporting structure of the TEH, is clamped onto a seismic shaker platform, while a tip mass ($M$) is affixed to the right end. The energy generation unit, comprising a stopper and a tribo-pair, rests atop the beam, separated by a spacer. The tribo-pair consists of two substrates: the upper substrate, fixed on the stopper's right end, bears a layer of PTFE film atop an aluminum (Al) electrode film, while the lower substrate, free to rotate about its left end, features a layer of copper (Cu) film on top, functioning as both the electrode and the triboelectric material with an electron affinity opposite to the PTFE film. The highly flexible soft-acrylic elastomer tape facilitates the lower substrate's free rotation about the left end. Subsequently, the right end of the lower substrate is connected to the beam near its right end via a connector affixed to the beam using a piece of Scotch tape. When

**Table 1**
Comparison of modeling approaches for TEHs.

| Study | Mechanical Model | EEC Model | Electromechanical Coupling in Model | System-Level Simulation | Modeling Platform |
|---|---|---|---|---|---|
| Niu & Wang (2015) [18] | Sinusoidal assumption | Nonlinear EECs | One-way coupling | Circuit-only | COMSOL |
| Fu et al. (2018) [25] | Nonlinear vibro-impact model | Lumped resistor | Two-way coupling | Not included | MATLAB |
| Pathak & Kumar (2021) [29] | Sinusoidal assumption | Nonlinear EECs | One-way coupling | Circuit-only | Circuit simulator |
| This study (Proposed ECM) | Nonlinear vibro-impact model | Nonlinear EECs | Two-way coupling | Included | Circuit simulator |

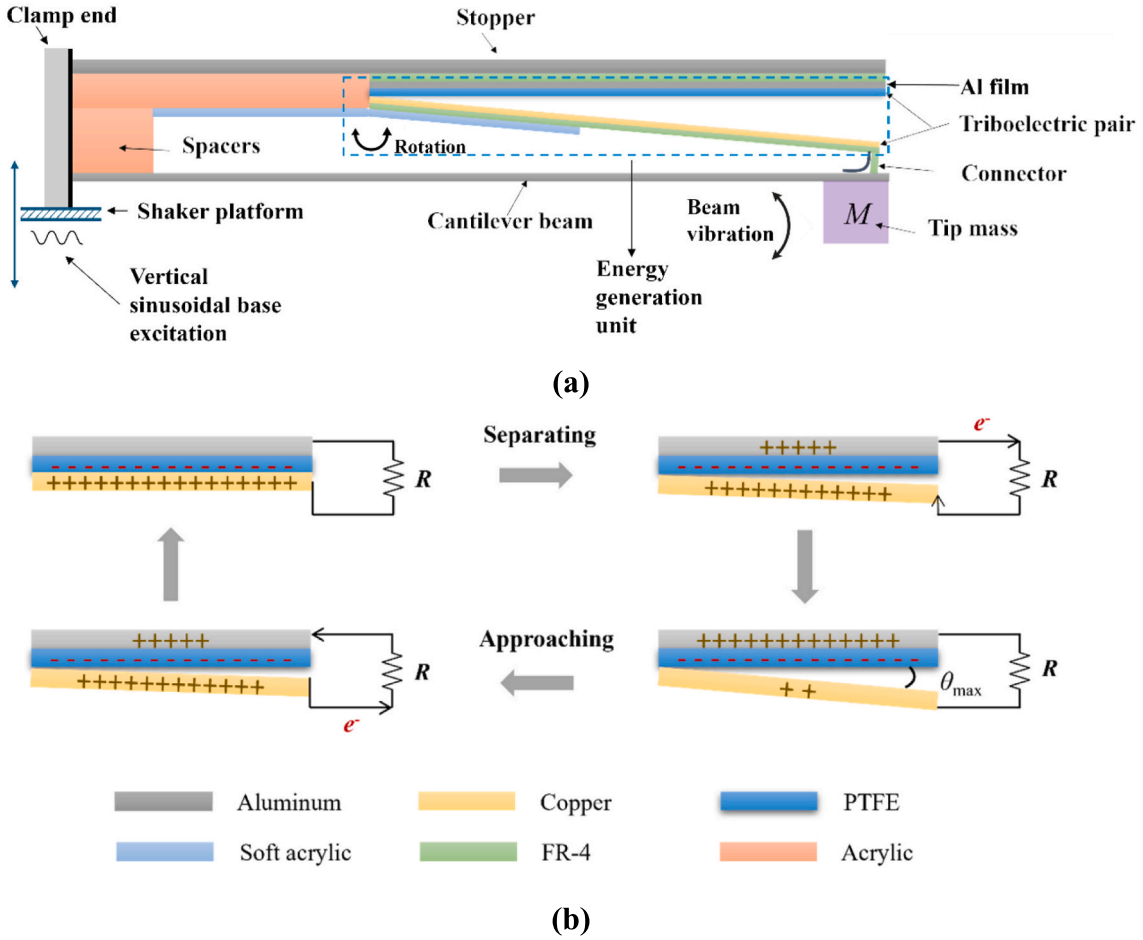


**Fig. 1.** (a) Structure of the TEH, and (b) its operating mechanism within the energy generation unit.

vertical sinusoidal base vibration is applied by the seismic shaker platform, cyclic contact and separation between the lower and upper substrates in the energy generation unit occur as the beam vibrates in response to the base excitation. When the Cu film on the lower substrate contacts the PTFE layer on the upper substrate, which is fixed to the stopper, a downward impact force is exerted on the lower substrate by the stopper. This impact force is transmitted to the tip of the beam through the connector. Since the impact force is applied to the beam only when the lower substrate contacts and sticks to the upper substrate, it acts as a nonlinear external force experienced by the cantilever beam during vibration.

Fig. 1 (b) depicts the operating mechanism of the electrical energy generation unit, with a resistor ($R$) connected to the Cu and Al layers, acting as electrodes. This non-parallel-plate configuration has been proven to ensure stable contact-separation cycles between the tribo-pair [24,26,41]. The initial state of the tribo-pair is illustrated in the top left corner of Fig. 1 (b), wherein the substrates are in contact, acquiring opposite charges [42]. The PTFE film, an insulator with high electron affinity, retains negative charges on its surface. As the lower substrate's positively charged Cu layer separates from the upper substrate's PTFE film while the beam deflects downward during vibration, an electric potential is induced in the air gap. Consequently, electrons flow due to the potential difference between the Al and Cu layers, neutralizing the positive charges on the Cu layer and imparting positive charges to the Al electrode. As the separation angle ($\theta$) between the substrates reaches its maximum, the transfer of negative charges to the Cu layer peaks. Subsequently, as the lower substrate moves up and reduces the gap, the potential inside the gap decreases, leading to a higher potential inside the PTFE dielectric layer than within the gap. This prompts negative charges to flow back to the Al layer until it becomes uncharged. This cyclical process results in alternating current flow across $R$ when repeated.

## 3. Electromechanical model of TEH

The electromechanical model presented in this section is based on previously validated work [24,43], in which the governing equations for a cantilever-based TEH operating in contact-separation mode were derived and experimentally verified. For clarity and completeness, we provide a concise summary of the model here to establish the foundation for the development of the ECM in the following sections. Accordingly, several equations are introduced without full derivation but are properly referenced to the original

sources for readers seeking a more detailed formulation.

While the underlying model structure follows our earlier studies, the present work differs significantly in its objectives and contributions. Specifically, this study focuses on translating the electromechanical model into an equivalent circuit representation that captures nonlinear interactions and enables system-level simulation using circuit simulation environments. Key innovations include the implementation of programmable arbitrary voltage sources to represent impact and electrostatic forces, the incorporation of pseudo-circuit elements to account for bidirectional electromechanical coupling, and the integration of practical EECs for experimental validation of system-level performance. These advancements constitute the principal novel contributions of the current work.

The TEH's electromechanical model comprises the electrical model of the tribo-pair and the mechanical model of the entire vibratory system. Fig. 2 illustrates the electrical model aimed at solving the voltage ($V$) across the external resistor ($R$) connected to the tribo-pair's electrodes. Kirchhoff's voltage law yields

$$V = V_d + V_a \tag{1}$$

where $V_d$ denotes the voltage inside the PTFE dielectric layer, and $V_a$ represents the voltage in the air gap. When the Cu electrode on the lower substrate makes contact with the PTFE layer above, negative charges accumulate on the surface of the PTFE layer, resulting in a charge density per unit area of $-\sigma$ due to triboelectrification. As the Cu electrode separates from the PTFE layer, it acquires negative charges $-Q$ that flow from the Al electrode above, driven by the voltage potential $V_a$ in the air gap. The voltage $V_d$, induced by the positive charges $Q$ accumulated on the Al electrode film, can be derived using Gauss's Law as follows

$$V_d = \frac{-Qh}{A_c \varepsilon_r \varepsilon_0} \tag{2}$$

where $h$ represents the PTFE's thickness, $A_c$ is the contact area between the tribo-pair, $\varepsilon_0$ is the permittivity of free space, and $\varepsilon_r$ is the PTFE's relative permittivity. The $V_a$ in the air gap can be calculated based on the total electric field energy, assuming equipotential conditions. The electric field lines are assumed to be perpendicular to the contact surfaces along the $l$-direction, allowing the electric field energy to be integrated as [43]

$$W_e = \int_{l_1-l_2}^{l_1} \frac{\varepsilon_0 E_a^2}{2} wl\theta dl = \int_{l_1-l_2}^{l_1} \frac{\varepsilon_0}{2}\left(\frac{V_a}{l\theta}\right)^2 wl\theta dl = \int_{l_1-l_2}^{l_1} \frac{\varepsilon_0 V_a^2 w}{2l\theta} dl = \frac{\varepsilon_0 V_a^2 w}{2\theta}\ln\left(\frac{l_1}{l_1-l_2}\right) \tag{3}$$

where $E_a$ is the electric field in the air gap that depends on $l$ due to the non-parallel configuration, $w$ is the width of the contact surfaces, $\theta$ is the separation angle between the contact surfaces, $l_1$ is the distance from the rotational end of the Cu electrode substrate to its outer end, and $l_2$ is the length of the contact surface between the triboelectric pair. The electric field energy $W_e$ is also related to the total capacitance in the air gap, $C$, by

$$W_e = \frac{CV_a^2}{2} = \frac{(\sigma A_c - Q)V_a}{2} \tag{4}$$

Equating the right-hand sides of Eq. (3) and Eq. (4) gives

$$V_a = \frac{\mu(\sigma A_c - Q)\theta}{w\epsilon_0} = \frac{\mu(\sigma A_c - Q)d_G}{wl_1\epsilon_0} \tag{5}$$

where $d_G$ represents the separation distance between the outer ends of the electrode substrates, and the small-angle approximation is applied here as $d_G \ll l_1$. In this context, $\mu$ is a geometric coefficient expressed as

$$\mu = \left[\ln\left(\frac{l_1}{l_1-l_2}\right)\right]^{-1} \tag{6}$$

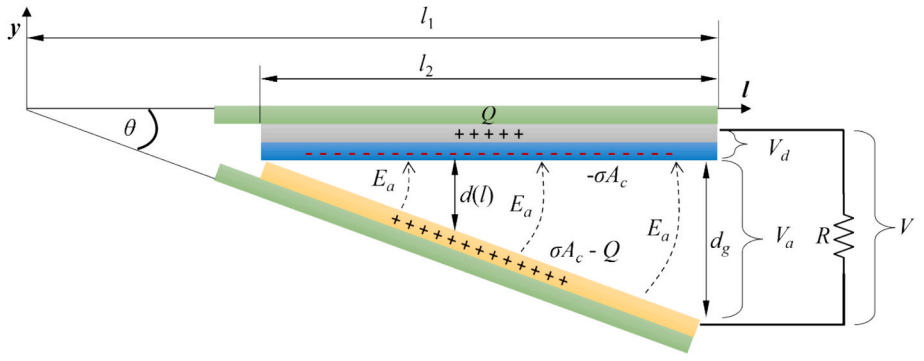


**Fig. 2.** Schematic diagram of the electrical model of the tribo-pair.

Substituting the expressions for $V$, $V_d$, and $V_a$ into the above equation, the governing equation for the transferred charge across $R$ is obtained as [43]

$$R\frac{dQ(t)}{dt}=\frac{\mu[\sigma A_c-Q(t)]d_g(t)}{wl_1\varepsilon_0}-\frac{Q(t)h}{A_c\varepsilon_r\varepsilon_0} \tag{7}$$

Eq. (7) can be rearranged as

$$R\frac{dQ(t)}{dt}=\frac{\mu\sigma A_c d_g(t)}{wl_1\varepsilon_0}-\frac{Q(t)}{\varepsilon_0}\left(\frac{h}{A_c\varepsilon_r}+\frac{\mu d_g(t)}{wl_1}\right) \tag{8}$$

where the first term on the right-hand side represents the open-circuit voltage induced by the separated triboelectric charges between the PTFE and the Cu layer [18], and the second term is the voltage caused by the internal capacitance between the Al and Cu electrodes [18]. The values of the electrical model's parameters utilized in the simulation and experiments conducted in this study are listed in Table 2.

The separation distance $d_g(t)$ serves as the coupling term linking the mechanical and electrical models, which will be elaborated upon later. The distributed-parameter mechanical model of the beam-mass-stopper system is outlined in Fig. 3. The right tip of the cantilever beam experiences impact due to the collision between the rotatable lower substrate and the upper substrate fixed on the mechanical stopper, as depicted in Fig. 1. This impact force essentially acts at the point where the connector is positioned in Fig. 1, enabling the simplification of the stopper into a spring-damper system with a constant stiffness ($K$) and damping coefficient ($C$), as illustrated in Fig. 3. The derivation of the mechanical model is based on Euler–Bernoulli beam theory, and the homogeneous governing equation for the free vibration of the beam without external forces is given by

$$\rho\frac{\partial^2}{\partial t^2}y(x,t)+EI\frac{\partial^4}{\partial x^4}y(x,t)=0 \tag{9}$$

where $\rho$, $E$, and $I$ represent the mass density per unit length, Young's modulus, and the second moment of area of the beam, respectively. The homogeneous form in Eq. (9) is presented to illustrate the modal decomposition prior to the inclusion of external forces. The complete modal equation incorporating external forces is introduced in the subsequent discussion. The beam is assumed to be a uniform Euler-Bernoulli beam. Employing the separation-of-variable method, $y(x, t)$ can be expressed as

$$y(x,t)=Y(x)\eta(t) \tag{10}$$

where $Y(x)$ represents the first-order modal shape, and $\eta(t)$ denotes the first modal coordinate. $Y(x)$ is expressed as

$$Y(x)=A(\sin\beta x-\sinh\beta x)+B(\cos\beta x-\cosh\beta x) \tag{11}$$

where $A$ and $B$ are constants determined from the boundary conditions of a cantilever beam with a tip mass and

$$\beta^4=\frac{\omega^2\rho}{EI} \tag{12}$$

where $\omega$ is the first modal natural frequency. It is important to note that only the contribution of the fundamental mode is considered in Eqs. (10) − (12), with higher-order modes being neglected due to their corresponding modal natural frequencies falling beyond the harvester's usual working frequency range. Incorporating modal damping, the modal equation is derived as

$$\frac{d^2}{dt^2}\eta+2\zeta\omega\frac{d}{dt}\eta+\omega^2\eta(t)=N(t) \tag{13}$$

where $\zeta$ is the modal damping ratio and $N(t)$ represents the modal external force expressed as [43]

$$N(t)=-\left[\rho\int_0^L Y(x)dx+MY(L)\right]\frac{d^2}{dt^2}y_v(t)+F_p(t)+F_e(t) \tag{14}$$

**Table 2**
Values of parameters for the electrical model.

| Parameters | Values |
|---|---|
| Permittivity of free space, $\varepsilon_0$ | $8.854\times10^{-12}$F·m$^{-1}$ |
| PTFE layer's relative permittivity, $\varepsilon_r$ | 2.1 |
| Thickness of PTFE layer, h | 0.18 mm |
| Length of contact surface, $l_2$ | 75 mm |
| Width of the contact surface, w | 40 mm |
| Area of the contact surface, $A_c$ | 3000 mm$^2$ |
| Constant coefficient, μ | 0.076 |

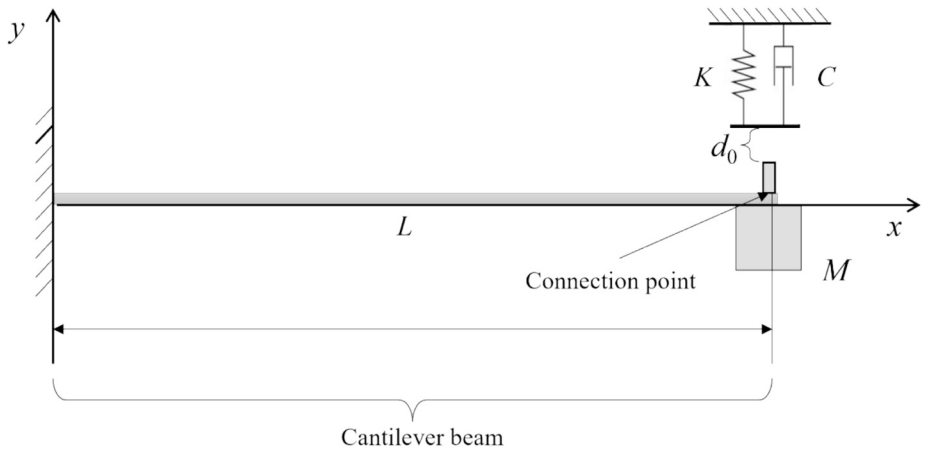


**Fig. 3.** Schematic diagram of the mechanical model for the beam-mass-stopper system.

Here, $L$ denotes the beam's length, $\ddot{y}_v(t)$ is the base excitation acceleration that can be provided by a seismic shaker, $F_p(t)$ is the modal impact force experienced by the beam's tip when impacting the stopper, and $F_e(t)$ is the modal electrostatic force arising from the opposite charges between the dielectric surface and the lower Cu electrode in Fig. 2. As the stopper is modeled as a spring-damper system in Fig. 3, the impact force $F_p(t)$ is expressed as [24,43]

$$F_p = \begin{cases} 0 & y(L,t) \leqslant d_0 \\ [K(d_0 - y(L,t)) - C\dot{y}(L,t)]Y(L) & y(L,t) > d_0 \end{cases} \tag{15}$$

where additional stiffness and damping coefficients are added when the impact occurs. In Eq. (15), the nonlinear contact force experienced by the beam during impact, referred to as the impact force $F_p$, acts in the direction normal to the contact surface and is therefore equivalent to the normal force $F_N$ in this configuration. The electrostatic force $F_e(t)$ is expressed as [24,43]

$$F_e(t) = \begin{cases} \dfrac{\mu l_2[\sigma A_c - Q(t)]^2 \cos(\theta)}{2 l_1 A_c \varepsilon_0} Y(L) & y(L,t) \leqslant d_0 \\ 0 & y(L,t) > d_0 \end{cases} \tag{16}$$

In Eq. (15), $d_0$ represents the initial separation distance between the right ends of the substrates in Fig. 2.

Given that the separation distance between the right ends of the substrates in Fig. 2, which is expressed as $d_g(t)$, couples the mechanical model to the electrical model, it is defined as the difference between the initial separation distance $d_0$ and the displacement of the beam's tip. Consequently, $d_g(t)$ is expressed as

$$d_g = \begin{cases} 0 & y(L,t) \geqslant d_0 \\ d_0 - y(L,t) & y(L,t) > d_0 \end{cases} \tag{17}$$

Furthermore, the coupling term from the electrical model in the mechanical model is the transferred charge $Q(t)$ in Eq. (16). The values of the mechanical parameters utilized in both simulation and experimentation are detailed in Table 3. In Table 3, the stopper's equivalent stiffness, $K$, was determined experimentally, while the damping coefficient, $C$, was empirically determined [24]. Since there is no straightforward method to determine $C$, an empirical value of 0.09 Ns/m was used [24]. However, $K$ is more crucial and has a much more significant influence on the dynamic response of the cantilever beam, so it needed to be determined experimentally. The details of how $K$ was determined will be explained in Section 5 below.

**Table 3**
Parametric values for the mechanical model.

| Parameters | Values |
|---|---|
| Length of beam, L | 105 mm |
| Young's Modulus of the beam, E | 69 GPa |
| Width of beam, b | 30 mm |
| Height of beam, $h_b$ | 1 mm |
| Mass density per unit length of the beam, ρ | 0.081 g/mm |
| Tip mass on beam, M | 30.77 g |
| Stopper's equivalent stiffness, K | 2500 |
| Stopper's equivalent damping coefficient, C | 0.09 |
| Initial separation distance, $d_0$ | 4.8 mm |

## 4. Equivalent circuit model of TEH

The derivation presented in the preceding paragraph simplifies the EEC of the electromechanical model by reducing it to a resistor. However, attempting to simulate the system-level response of TEHs based solely on analytical formulas becomes exceedingly challenging, if not impossible, especially when considering more sophisticated EEC interfaces beyond a simple resistor. The complexity arises from the intricate interplay of the electromechanical model's bidirectional coupling, the inherent nonlinearity of TEHs, and the complex nonlinear circuit interfaces they may be connected to. Nevertheless, conducting system-level simulations for TEHs with intricate circuit interfaces is feasible using circuit simulation software, provided that the ECM of the TEH's electromechanical model is translated into its circuit equivalent. In fact, the ECM has been widely employed to assess the performance of PEHs [34,36], yet its application in evaluating the electromechanical response of TEH systems remains unexplored. One significant challenge lies in the distinct analytical formulation required for TEHs compared to PEHs, given their distinct coupling and power generation mechanisms. Unlike PEHs, which typically exhibit linear electromechanical behavior [44], TEHs demonstrate nonlinear characteristics [25], further complicated by vibro-impact-induced nonidealities and intricate coupling behaviors. Consequently, constructing an electromechanical model for a TEH system featuring a nonlinear EEC becomes arduous, particularly for conventional simulation techniques like MATLAB programming. This section demonstrates how, for the first time, the ECM for the TEH system can be identified and developed, enabling comprehensive system-level simulation of its mechanical, electrical, and EEC components using circuit simulation tools such as PSpice, Simetrix, Simulink, and Simscape.

Before presenting the derivation, it is important to clarify that the ECM representation of the electromechanical subsystem is directly derived from the same governing equations outlined in Section 3, consistent with those used in conventional mathematical modeling. As a result, the modeling assumptions, simplifications, and computational complexity are effectively the same. Therefore, the ECM does not inherently offer faster computation when applied to the electromechanical model in isolation. Its practical value lies in enabling the simulation of fully coupled TEH systems, incorporating both nonlinear mechanical dynamics and complex energy extraction circuitry, within a unified circuit simulation environment. This integration facilitates system-level analysis and co-optimization in ways that are difficult to achieve using traditional ODE-based co-simulation approaches.

### 4.1. ECM of mechanical model

The mechanical model presented in the previous section consists of Eqs. (13)-(17), the circuit analogies of which need to be identified for formulating the ECM. The modal equation of motion in Eq. (13) shares the same structure as the response equation of an RLC circuit subjected to an external voltage source, expressed as

$$L_{eq}\frac{d^2}{dt^2}q(t)+R_{eq}\frac{d}{dt}q(t)+\frac{1}{C_{eq}}q(t)=V_N(t) \tag{18}$$

where $L_{eq}$ is the inductor, $R_{eq}$ is the resistor, $C_{eq}$ is the capacitor, $q(t)$ is the charge that flows through the RLC circuit, and $V_N(t)$ is the external voltage source for the circuit. Dividing both sides of Eq. (18) by $L_{eq}$ gives

$$\frac{d^2}{dt^2}q(t)+\frac{Q_{RLC}}{\omega}\frac{d}{dt}q(t)+\omega^2 q(t)=\frac{V_N(t)}{L_{eq}} \tag{19}$$

where

$$Q_{RLC}=\frac{1}{R_{eq}}\sqrt{\frac{L_{eq}}{C_{eq}}} \tag{20}$$

$$\omega=\frac{1}{\sqrt{L_{eq}C_{eq}}} \tag{21}$$

Here, $Q_{RLC}$ denotes the quality factor of the equivalent RLC circuit, and $\omega$ is the natural frequency of the RLC circuit, which is the same as $\omega$ in the cantilever beam's modal dynamical equation in Eq. (13). A comparison between Eqs. (13) and (18) or between Eqs. (13) and (19) reveals that in the equivalent forced RLC circuit, the modal external force $N(t)$ is equivalent to an external voltage source $V_N(t)$, and the modal displacement $\eta(t)$ is equivalent to the charge $q(t)$ flowing in the circuit. Additionally, the inductance of the equivalent inductor $L_{eq}$ equals the constant coefficient 1 of $\ddot{\eta}(t)$, the resistance of the equivalent resistor $R_{eq}$ equals $2\zeta\omega$, and the capacitance of the equivalent capacitor $C_{eq}$ equals $\omega^{-2}$. The modal external force in Eq. (14) consists of the modal base excitation force $-\left[\rho\int_0^L Y(x)dx+MY(L)\right]\ddot{y}_v(t)$, the modal impact force $F_p(t)$, and the modal electrostatic force $F_e(t)$. Hence, using the analogy to Eq. (14), the external voltage source $V_N(t)$ can be expressed as

$$V_N(t)=-\left[\rho\int_0^L Y(x)dx+MY(L)\right]V_v(t)+V_p(t)+V_e(t) \tag{22}$$

where $V_v(t)$ represents the excitation voltage source, $V_p(t)$ is equivalent to $F_p(t)$, and $V_e(t)$ is equivalent to $F_e(t)$. Since $\eta(t)$ has been

identified as equivalent to $q(t)$ in the RLC circuit, $V_p(t)$ can be expressed as

$$V_p = \begin{cases} 0 & Y(L)q(t) \leqslant d_0 \\ K[d_0 - Y(L)q(t)]Y(L) - CY^2(L)\dfrac{d}{dt}q(t) & Y(L)q(t) > d_0 \end{cases} \tag{23}$$

$V_e(t)$ is expressed as

$$V_e(t) = \begin{cases} \dfrac{\mu l_2[\sigma A_c - Q(t)]^2\cos(\theta)}{2l_1 A_c \epsilon_0} Y(L) & Y(L)q(t) \leqslant d_0 \\ 0 & Y(L)q(t) > d_0 \end{cases} \tag{24}$$

where $Q(t)$ denotes the charge in the equivalent circuit for the electrical model, and $\theta$ is

$$\theta = \arcsin\left(\frac{d_g(t)}{l_1}\right) \tag{25}$$

where

$$d_G = \begin{cases} 0 & Y(L)q(t) \geqslant d_0 \\ d_0 - Y(L)q(t) & Y(L)q(t) < d_0 \end{cases} \tag{26}$$

To represent external forces in the ECM, programmable arbitrary voltage sources are introduced. For example, in Eq. (23), the impact force $F_p$ is represented by the voltage source $V_p$. This source reproduces the time-varying behavior of $F_p$, derived from the mechanical model, and serves as the input to the circuit branch corresponding to the mechanical subsystem. By implementing $F_p$ as a time-dependent voltage source, the ECM can emulate the nonlinear and transient nature of impact within a circuit simulation environment. Since the normal force $F_N$ is equivalent to $F_p$ in this context, no separate voltage source is required to represent $F_N$, and the impact dynamics are fully captured through $V_p$.

Once the electrical and circuit equivalents of the mechanical parameters listed in Table 4 are identified, the ECM for the mechanical model (M−ECM) can be established. The schematic diagram of the M−ECM, drawn in the circuit simulator Simetrix, is illustrated in Fig. 4. Simetrix is preferred over other tools like Simscape or PSpice due to its suitability for this study's objectives, straightforward user interface, fast and stable numerical solvers, and easily interpretable circuit diagrams. In Fig. 4, the equivalent inductor $L_{eq}$, capacitor $C_{eq}$, and resistor $R_{eq}$ are connected in series. Additionally, the three voltage sources connected in series are the sinusoidal voltage source $V_v$, the voltage source $V_e$, which is equivalent to the electrostatic force $F_e$, and the voltage source $V_p$, which is equivalent to the impact force $F_p$. In this configuration, $V_e$ and $V_p$ are arbitrarily defined differential voltage sources capable of accepting voltage and current inputs. The symbols OUTP and OUTN in $V_e$ and $V_p$ denote positive and negative outputs, respectively. The expression for $V_e$ in Eq. (24) includes $d_G$ as expressed in Eq. (26), involving the equivalent charge $q(t)$ flowing in the circuit. Thus, the arbitrary source $V_e$ must monitor the voltage across the equivalent capacitor $C_{eq}$ so that $q(t)$ can be calculated as

$$q(t) = C_{eq}V_C(\text{in}\backslash\text{\_a},\ \text{in}\backslash\text{\_b}) \tag{27}$$

where $V_C$(in_a, in_b) is the voltage across $C_{eq}$. The electric wires stemming from the voltage input ports in_a and in_b of $V_e$ probe $V_C$ across $C_{eq}$ and utilize its probed value as the input for $V_e$. Similarly, as the expression for $V_p$ in Eq. (23) involves $q(t)$, the arbitrary voltage source $V_p$ in Fig. 4 also includes two wires stemming from its in_a and in_b ports to probe $V_C$ and utilize its value as one input. Additionally, due to the dependency of Eq. (23) on $\dot{q}(t)$, $V_p$ also probes the equivalent current $\dot{q}(t)$ flowing in the circuit and utilizes it as its input, denoted as I(in). It is crucial to note that, as per Eq. (24), another variable input required in $V_e$, namely the transferred charge between the tribo-pair $Q(t)$, has not yet been integrated into the schematic diagram in Fig. 4. This inclusion will be addressed when the ECM for the electrical model (E-ECM) is developed in the subsequent subsection.

### 4.2. ECM of electrical model

The establishment of the M−ECM addresses only a portion of the electromechanical model of the TEH. This subsection outlines the procedures for constructing the E-ECM. As per Eq. (8), the governing equation for the transferred charge across a resistor connected to

**Table 4**
Mechanical parameters and their electrical circuit analogies.

| Mechanical parameters | Equivalent circuit parameters |
|---|---|
| Modal displacement, $\eta(t)$ | Charge, $q(t)$ |
| Modal velocity, $\dot{\eta}(t)$ | Current, $\dot{q}(t)$ |
| Coefficient of $\eta(t)$, 1 | Inductance, $L_{eq}$ |
| Effective modal damping, $2\zeta\omega$ | Resistance, $R_{eq}$ |
| The inverse of effective modal stiffness, $\omega^{-2}$ | Capacitance, $C_{eq}$ |
| Base excitatory acceleration, $\ddot{y}_v(t)$ | Excitatory voltage source, $V_v(t)$ |

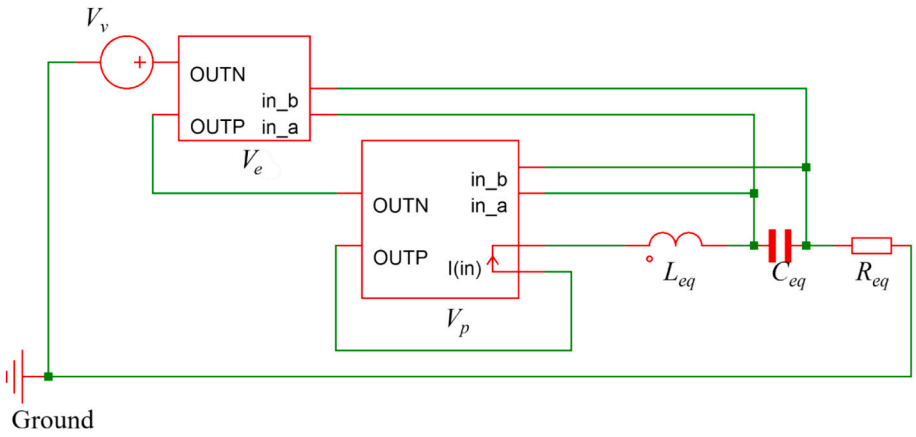


**Fig. 4.** Schematic diagram of the M−ECM in Simetrix.

a TEH, the output voltage on an external resistor is the difference between the open-circuit voltage due to the triboelectric charges, $V_{oc}$, and the voltage $V_{ic}$ due to the tribo-pair's inherent capacitance, $C_{ic}$ [18]. These two terms are expressed as

$$V_{oc} = \frac{\mu\sigma A_c d_g(t)}{wl_1\varepsilon_0} \tag{28}$$

$$V_{ic} = \frac{Q(t)}{\varepsilon_0}\left(\frac{h}{A_c\varepsilon_r} + \frac{\mu d_g(t)}{wl_1}\right) \tag{29}$$

The E-ECM [18] is depicted in Fig. 5. In practical applications involving more complex EECs, the resistor $R$ can be substituted with the circuit models of the EECs for simulation purposes. The two equivalent voltage sources in the E-ECM, $V_{oc}$ and $V_{ic}$, are nonlinear. Therefore, they must be programmed into arbitrary differential voltage sources in the circuit simulator, akin to the ones for $V_e$ and $V_p$ in the M−ECM in Fig. 4. Fig. 6 illustrates the actual diagram of the E-ECM used in the simulator. In the circuit simulator, the arbitrary source for $V_{ic}$ necessitates the amount of charge flowing across $R$ in Fig. 5, $Q(t)$, as its input. However, the arbitrary source in the circuit simulator cannot directly monitor the charge flowing in the circuit since most circuit simulators' programmable arbitrary voltage sources only accept voltage and current as their inputs. This issue is addressed by employing an arbitrary current source $I_c$ and a pseudo-capacitor $C_i$, which serve the sole mathematical purpose of calculating the charge $Q(t)$, shown in Fig. 6. $I_c$ probes the value of the current flowing in the circuit, denoted by $I(t)$ in the component block of $I_c$, and outputs that current with the same magnitude into the pseudo-capacitor, $C_i$. The voltage across $C_i$ is then

$$V_i(t) = C_i\int_0^t I_c(\tau)d\tau \tag{30}$$

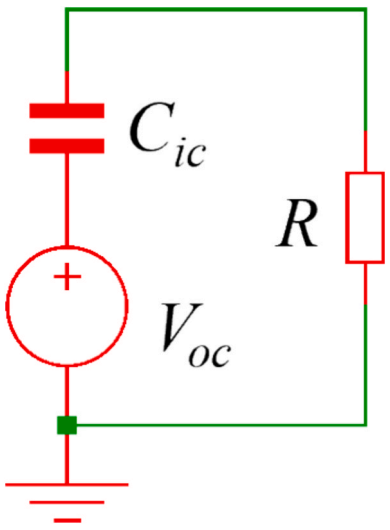


**Fig. 5.** Schematic diagram of the E-ECM.

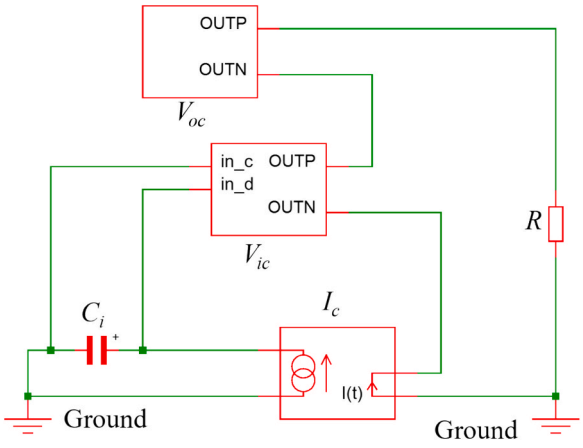


**Fig. 6.** Diagram of the E-ECM in Simetrix.

The value of $V_i(t)$ is then utilized as one of the inputs of $V_{ic}$ through ports in_c and in_d. The value of $Q(t)$ can subsequently be computed as

$$Q(t) = C_i V_i(t) \tag{31}$$

This value can then be programmed into the expression for $V_{ic}$ in the component block of the arbitrary voltage source.

As illustrated in Fig. 7, the comprehensive ECM of the TEH can be constructed by integrating the established M−ECM and E-ECM. Both $V_{oc}$ and $V_{ic}$ necessitate the value of $q(t)$ due to the inclusion of the term for the separation distance $d_g(t)$ in Eqs. (28) and (29), which encompasses the displacement-equivalent term $Y(L)q(t)$. Consequently, the two arbitrary voltage sources, $V_{oc}$ and $V_{ic}$, depicted in Fig. 6, require additional ports to probe the voltage across $C_{eq}$ in Fig. 4 to compute the equivalent charge $q(t)$. In Fig. 7, both $V_{oc}$ and $V_{ic}$ are equipped with input ports in_a and in_b to probe the voltage across $C_{eq}$ for the calculation of $q(t)$. Moreover, the arbitrary voltage source $V_e$ in Fig. 4 necessitates extra ports to probe the voltage across the integrator capacitor $C_i$ in Fig. 6 due to the presence of the term for the transferred charge $Q(t)$ in Eq. (24). Consequently, the equivalent voltage sources $V_e$ and $V_{ic}$ both possess input ports in_c and in_d

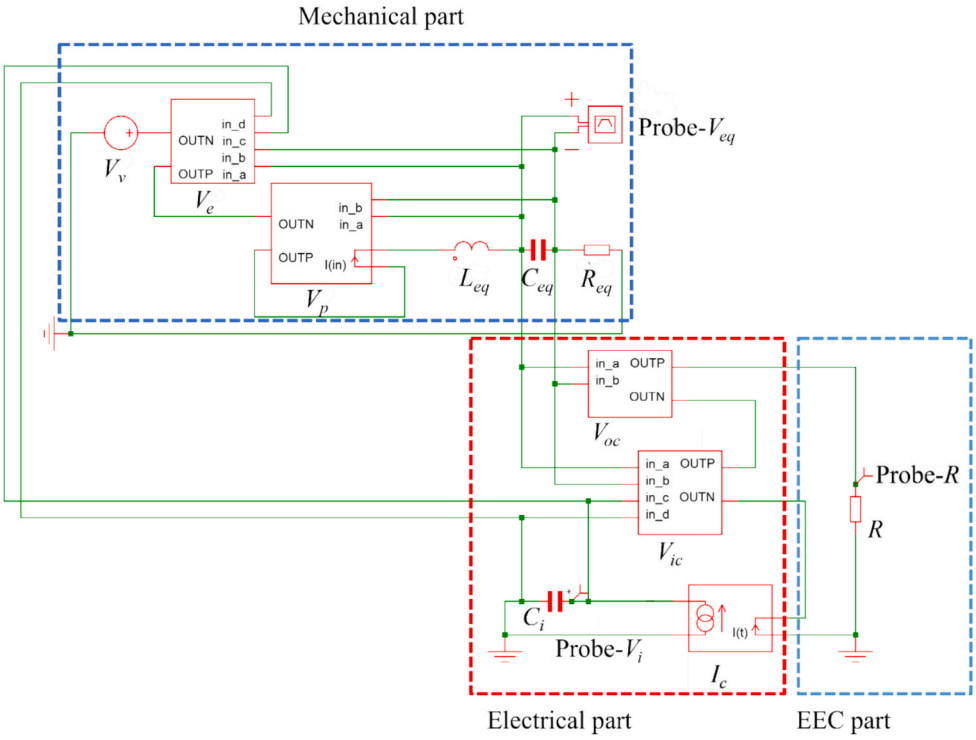


**Fig. 7.** Complete diagram of the ECM for TEH.

to probe the voltage across the pseudo-capacitor $C_i$ for the calculation of $Q(t)$.

## 5. Experimental validation of proposed ECM

This section introduces experimental case studies aimed at validating the proposed ECM. The first case study focuses on validating the ECM equivalent of the TEH's electromechanical model by assessing the voltage response across a resistor connected to the electrodes of the TEH in both time and frequency domains. Subsequently, the second case study verifies the DC voltage response and resistance matching for optimal output power. In this latter case, the external resistor is substituted with a nonlinear rectifying EEC to demonstrate the ECM's capability to facilitate system-level simulations under complex electromechanical conditions and practical EEC configurations. The parameters of the TEH are detailed in Table 2 and Table 3.

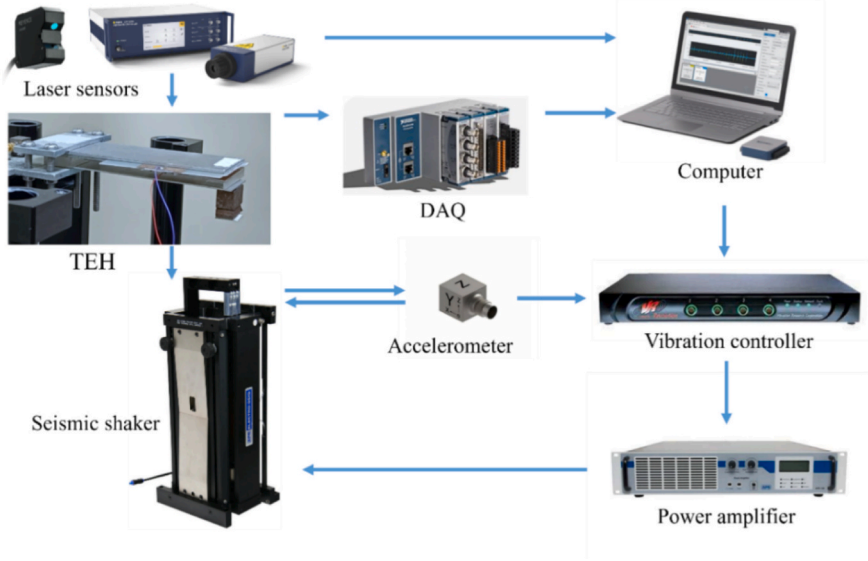


(a)

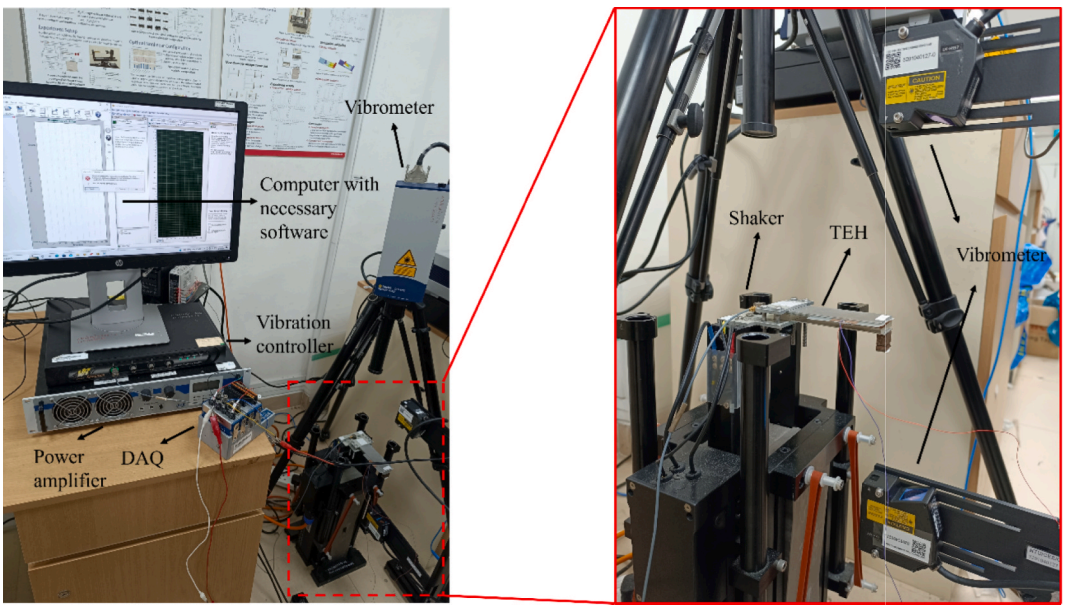


(b)

**Fig. 8.** (a) Graphical Illustration and (b) actual setup of experimental validation.

### 5.1. Experimental case study 1

This validation case study aims to confirm whether the ECM can simulate the TEH's response based on its electromechanical model without involving a complex EEC. Consequently, the EEC is simplified to a resistor $R$, as depicted in Fig. 7. The experimental setup, illustrated in Fig. 8, involves a seismic shaker that supplies vertical base vibrations to the TEH fixed on its platform. An accelerometer affixed to the shaker's platform provides feedback to a computer for vibration control via a vibration controller linked to the computer. Vibration control is managed using a custom program synchronized with the vibration controller, while a power amplifier amplifies the vibration-controlling signal. The TEH connects to a data acquisition (DAQ) module through two conducting wires from its electrodes. The resistance $R$ in Fig. 7 is 1 MΩ because the DAQ module has a built-in resistance of 1 MΩ. In addition, two sets of laser vibrometers are used to measure the displacement of the shaker's platform and the tip displacements of the beam and the TEH's stopper. The voltage signals proportional to the displacement detected are also acquired by the DAQ module.

The electromechanical model of the TEH describes the $V$-$Q$-$x$ relationship in the time domain [19], where $V$ represents the voltage across the resistor, $Q$ denotes the transferred charge, and $x$ signifies the displacement. In this investigation, $Q$ corresponds to the positive charge transferred to the Al electrode, $Q(t)$, as depicted in the electrical model in Fig. 2. At the same time, $x$ correlates with the beam's tip displacement, $y(L, t)$, as illustrated in the mechanical model in Fig. 3. Consequently, this relationship is relabeled as the $V$-$Q$-

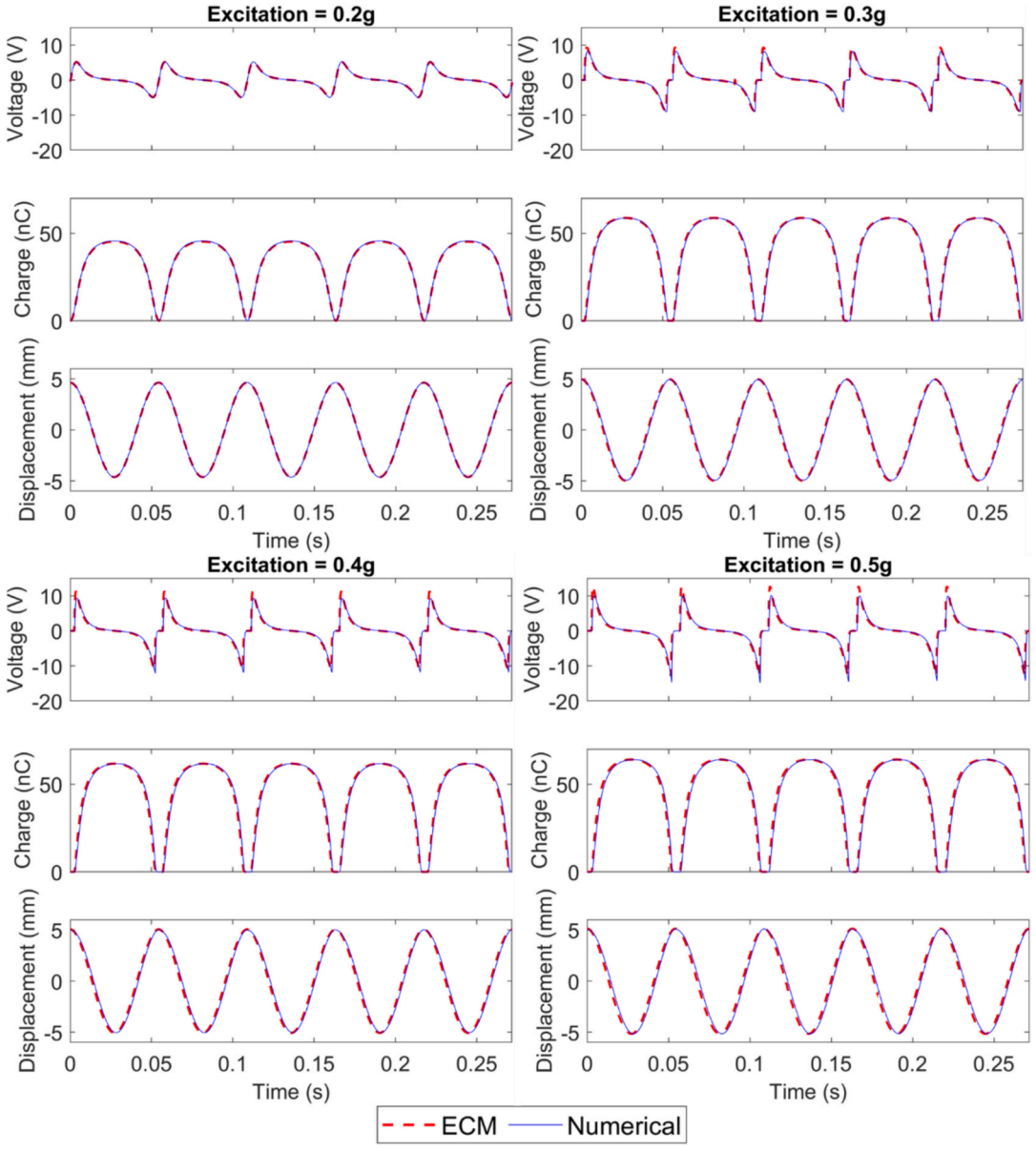


**Fig. 9.** $V(t)$, $Q(t)$, and $y(L, t)$ from ECM and numerical simulations at 18.4 Hz under base accelerations of 0.2 g, 0.3 g, 0.4 g, and 0.5 g.

$y$ relationship for this study. Within the ECM, $Q(t)$ is the product of the capacitance of the pseudo-capacitor, $C_i$, and the voltage across it, $V_i(t)$, as per Eq. Hence, it's crucial to probe the voltage across $C_i$, accomplished via the voltage probe labeled Probe-$V_i$ in Fig. 7. Similarly, $y(L, t) = Y(L)\eta(t) = Y(L)q(t)$ necessitates the voltage across $C_{eq}$. Consequently, $y(L, t)$ can be derived as $Y(L)C_{eq}V_{eq}(t)$, where $Y(L)$ represents the value of the modal shape at $x = L$ in Fig. 3, and $V_{eq}(t)$ denotes the equivalent voltage across $C_{eq}$. Probe-$V_{eq}$ is positioned across $C_{eq}$ to gauge $V_{eq}$. Furthermore, the voltage $V(t)$ across $R$ is easily measured by Probe-$R$ in Fig. 7. Simulation data acquired from the circuit simulator, Simetrix, comprise voltage forms $V(t)$, $V_i(t)$, and $V_{eq}(t)$, necessitating processing to transform the latter two into $Q(t)$ according to Eq. (31) and $y(L, t)$ according to the following

$$y(L,t) = Y(L)C_{eq}V_{eq}(t) \tag{32}$$

Because the TEH's ECM is strictly equivalent to the governing equations of the TEH's electromechanical model, namely Eqs. (8) and (13), the simulation results of the $V$-$Q$-$y$ relationship from the ECM should closely match those from numerical simulations. We conducted a comparison of the $V$-$Q$-$y$ relationships in the time domain from the ECM and numerical simulations near the undamped natural frequency of the TEH (18.59 Hz) at an excitation frequency of 18.4 Hz, with excitation levels ranging from 0.2 g to 0.5 g in 0.1 g increments. The results, shown in Fig. 9, demonstrate a close match between the ECM and numerical simulations, thus proving the equivalence between the ECM and the electromechanical model. In the experiment, $V(t)$ and the displacement $y(L, t)$ are obtained via the DAQ module, while the transferred charge, $Q(t)$, is computed from the $V(t)$ data as

$$Q(t) = \frac{1}{R}\int_0^t V(\tau)d\tau \tag{33}$$

Before presenting the experimental validation results, it is essential to explain how the stopper's stiffness, $K$, shown in Fig. 3, was determined experimentally. The determination of $K$ was carried out by adjusting its value in the ECM while keeping all other parameters fixed until the predicted displacement $y(L, t)$ of the beam's tip at a given excitation level and frequency aligned with the experimental result. If $K$ is too small, the beam experiences a prolonged sticking motion with the stopper; if $K$ is too large, the beam instantly bounces downwards. Therefore, the value of $K$ in the ECM directly influences the shape of the simulated $y(L, t)$ waveform. In this study, $K$ was specifically determined using the experimental data of the beam's tip displacement at 0.4 g excitation and 18.4 Hz excitation frequency, which is close to the undamped natural frequency of 18.59 Hz for the TEH.

Fig. 10 shows comparisons between the ECM-simulated $y(L, t)$ at three different $K$ values and the experimentally obtained $y(L, t)$ at 0.4 g excitation and 18.4 Hz excitation frequency. Two periods of oscillation are displayed, with the waveforms aligned in phase. The

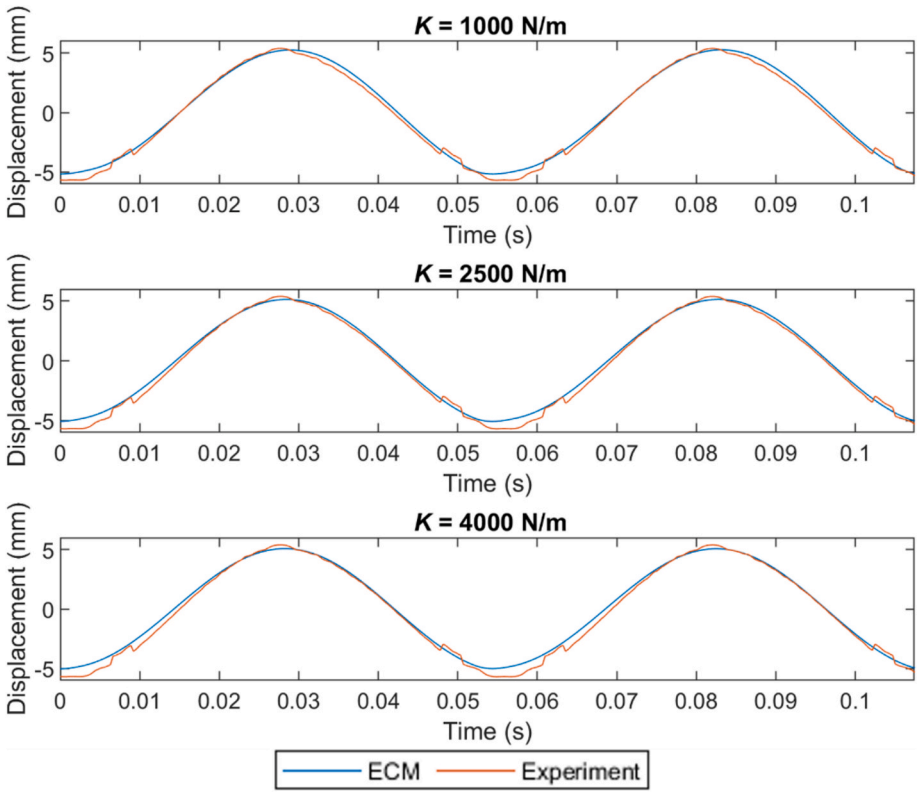


**Fig. 10.** Comparison of the ECM-simulated displacement response of the TEH using three different values of stopper stiffness, $K$, with the experimentally obtained displacement response.

three different input values of $K$ are 1000 N/m, 2500 N/m, and 4000 N/m. It is evident that when $K = 1000$ N/m, the ECM-simulated $y(L, t)$ descends later than the experimental $y(L, t)$ after reaching the maximum, due to the longer sticking motion between the stopper and the beam. Conversely, when $K = 4000$ N/m, the ECM-simulated $y(L, t)$ starts ascending much earlier than the experimentally obtained $y(L, t)$ after reaching the minimum, because the beam experiences a much shorter sticking motion with the stopper, causing it to bounce down prematurely and reach the minimum faster. After several adjustments, it was found that $K = 2500$ N/m provided the best match between the ECM-simulated and experimental displacements $y(L, t)$.

It is important to note that the experimentally determined value of the stopper's stiffness $K$ may be subject to certain uncertainties. One potential source of error arises from the displacement measurements—while laser vibrometers offer high precision, they can be influenced by factors such as surface reflectivity and alignment tolerances. Additionally, fabrication imperfections in the stopper or connector assembly, including minor variations in material stiffness, bonding conditions, or alignment, may lead to slight deviations from the idealized spring-damper behavior assumed in the model. Moreover, nonlinear contact phenomena—such as localized deformation, micro-slip, or hysteresis at the impact interface—are not fully captured by a linear spring-damper representation. These factors may result in slight variations in the effective stiffness experienced by the system during dynamic operation and contribute to residual discrepancies between simulation and experimental results, particularly under higher excitation levels where impact effects become more pronounced.

In both the experiment and simulation, the TEH undergoes base vibration at a frequency of 18.4 Hz, close to its undamped natural frequency of 18.59 Hz, with base excitation accelerations ranging from 0.2 g to 0.5 g at 0.1 g increments. The effective charge density $\sigma$ and the modal damping ratio $\zeta$ were determined experimentally and are listed in Table 5, along with the values of the equivalent LRC components. The modal damping ratio $\zeta$ can be easily derived using the logarithmic decrement method. However, while an increased modal damping ratio $\zeta$ was anticipated with increasing base excitation, the measured values varied negligibly. As a result, a constant $\zeta$ calculated from averaging the measured values is employed here.

Regarding the areal charge density $\sigma$, we assumed it to be the effective areal charge density, uniformly distributed across the PTFE surface, and estimated it using an electrometer. Specifically, the external resistor $R$ was replaced with an electrometer capable of measuring the transferred charge $Q$. Higher base excitation accelerations from the seismic shaker promoted more complete contact between the tribo-pair, resulting in increased charge transfer. The maximum transferred charge $Q_{max}$ was recorded at various excitation levels ranging from 0.2 g to 0.5 g. This charge was then divided by the contact area $A_c$ to calculate $\sigma$ for each excitation level, as reported in Table 5. Notably, the experimentally determined effective charge density $\sigma$ increases with excitation due to improved contact conditions, while at lower excitation levels, imperfect contact leads to reduced charge transfer.

Although this estimation method is practical, several factors may affect its accuracy. Direct quantification of the actual surface charge distribution on the PTFE is extremely challenging due to the dielectric's insulating nature and the inherent non-uniformity of triboelectric charge accumulation. Consequently, measuring the true areal charge density with standard laboratory equipment is impractical. Instead, we adopted an effective estimation approach based on the net transferred charge and the known contact area. The accuracy of this method is limited by factors such as inconsistent or incomplete contact between the tribo-pair, especially under lower excitation conditions, non-uniform surface charge distribution, and the resolution limits of the electrometer. In particular, fabrication tolerances in the TEH can result in imperfect alignment and contact between the PTFE and Cu electrode, further contributing to incomplete charge transfer. Despite these limitations, the estimated $\sigma$ values provide a reliable basis for calibrating the ECM across different excitation levels, enabling accurate reflection of the TEH's electromechanical behavior under varying operating conditions.

These findings are illustrated in Fig. 11, which compares the ECM-simulated and experimentally obtained voltage $V(t)$ and displacement $y(L, t)$ in the time domain. A strong correlation is observed between the ECM simulation results and experimental data for the $V$-$Q$-$y$ relationship, affirming the ECM's ability to accurately capture the TEH's electromechanical response in the time domain. The absolute peaks of both $V(t)$ and $Q(t)$ rise with increasing base acceleration due to the augmented kinetic energy availability. However, the increase in the absolute displacement $y(L, t)$ is less pronounced because the mechanical stopper constrains the maximum distance the beam's tip can travel in the positive direction.

While the simulated results for $V(t)$ generally align well with experimental data, noticeable deviations occasionally occur. These discrepancies can be attributed to several factors. A primary source is the nonlinear impact behavior between the tribo-pair, which is difficult to model precisely. Since the transferred charge $Q(t)$, which can drop abruptly during contact events, directly influences $V(t)$ through its rate of change, the voltage response is highly sensitive to variations in $Q(t)$ changes over time. As a result, even when the simulated $Q(t)$ closely matches experimental data, deviations in $V(t)$ may still appear more prominently.

Additional discrepancies in $V(t)$ may arise from experimental noise and the limited resolution of the voltage measurement system, especially during sharp transitions. Fabrication tolerances, constrained by the precision of laboratory tools, can also impact the consistency of contact between the tribo-pair, introducing instability and irregularities in the voltage waveform that are difficult to capture in the ECM. Moreover, the ECM employs a linear spring-damper representation of impact, whereas the actual contact dynamics

**Table 5**
Experimentally determined parameters and equivalent circuit parameters.

| $\ddot{y}_v$ | σ | ζ | $L_{eq}$ | $R_{eq}$ | $C_{eq}$ |
|---|---|---|---|---|---|
| 0.2 g | 20.00 μC/m$^2$ | 1.30 % | 1H | 3.04 Ω | 73.32 μF |
| 0.3 g | 21.83 μC/m$^2$ | 1.30 % | 1H | 3.04 Ω | 73.32 μF |
| 0.4 g | 22.93 μC/m$^2$ | 1.30 % | 1H | 3.04 Ω | 73.32 μF |
| 0.5 g | 23.77 μC/m$^2$ | 1.30 % | 1H | 3.04 Ω | 73.32 μF |

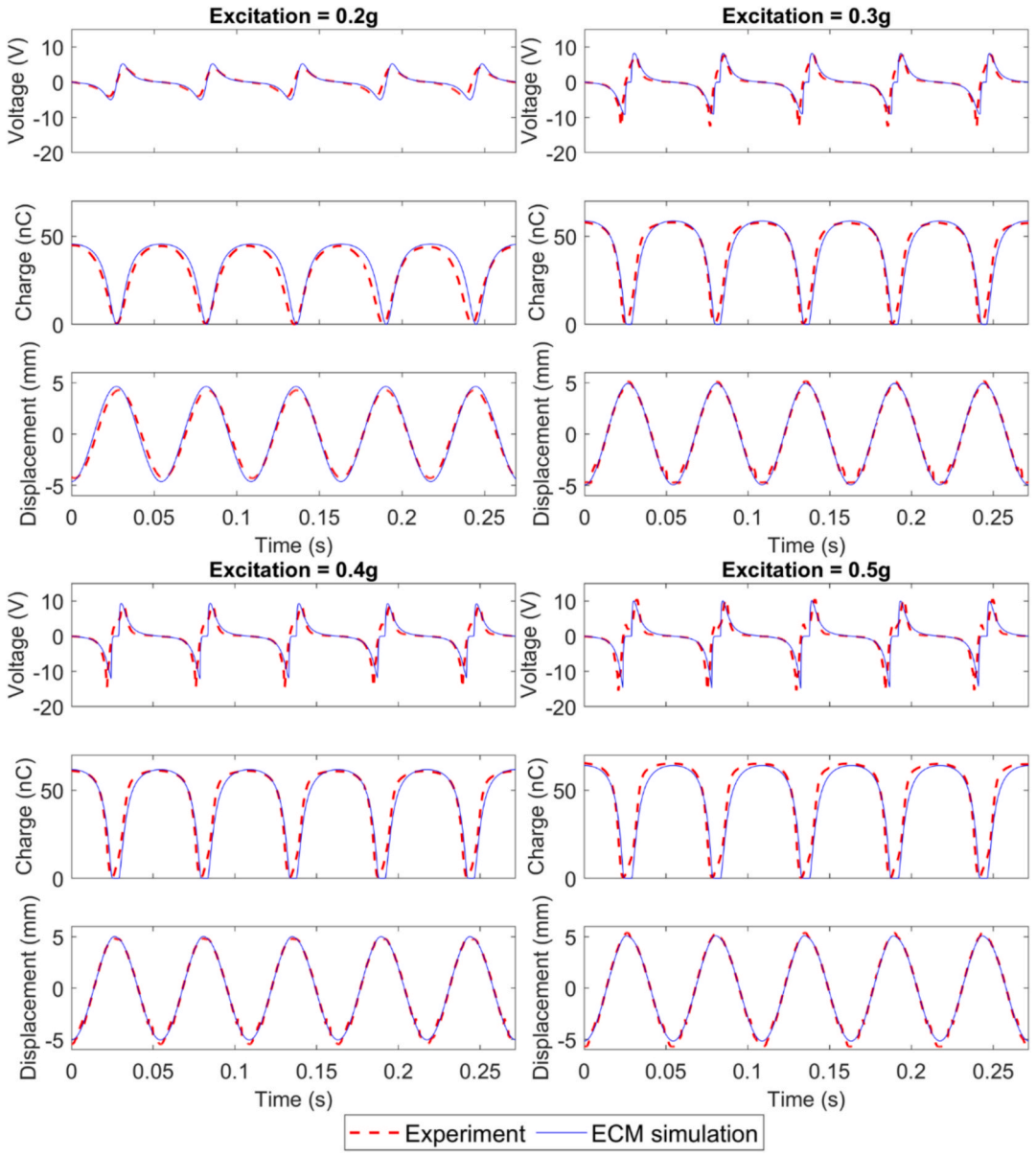


**Fig. 11.** $V(t)$, $Q(t)$, and $y(L, t)$ from the ECM simulation and experiment at 18.4 Hz under base accelerations of 0.2 g, 0.3 g, 0.4 g, and 0.5 g.

may involve unmodeled nonlinearities such as asymmetric impact forces, hysteresis, or localized deformation. These effects can lead to phase shifts or transient peaks in the voltage response. Despite these limitations, the ECM effectively captures the overall electro-mechanical behavior of the system and replicates key trends—particularly in displacement and charge responses—thereby validating its utility for system-level simulation and analysis.

The *V*-*Q*-*y* response obtained from the ECM simulation provides insights into the power-generation mechanism depicted in Fig. 1 (b). In Fig. 12 (a), two periods of the *V*-*Q*-*y* response, obtained from the ECM simulation when a base acceleration of 0.4 g at 18.4 Hz is applied to the TEH, are shown. The first period in Fig. 12 (a) is subdivided into three stages: I, II, and III, each corresponding to distinct phases of the TEH's operational mechanism. In stage I, as the beam's tip ascends, leading to an increase in $y(L, t)$, the gap between the triboelectric materials diminishes. Consequently, positive charges transfer from the Al electrode to the Cu electrode, resulting in a decrease in $Q(t)$. This decline in $Q(t)$ induces a negative voltage peak proportional to the slope of $Q(t)$. Stage II marks the point where $y(L, t)$ achieves its positive peak, bringing the triboelectric materials into contact. During this phase, the Cu electrode's substrate plate adheres to the stopper, maintaining the voltage at zero due to the absence of charge transfer while the materials are in contact. With the PTFE layer in contact with the Cu electrode, all positive charges transfer to the Cu electrode, leading to simultaneous decreases in $Q(t)$ and $V(t)$ until both reach zero. Subsequently, in stage III, the beam's tip descends after impact, causing the tribo-pair to separate. Positive charges are once again transferred to the Al electrode, resulting in an increase in $Q(t)$ and a positive voltage peak.

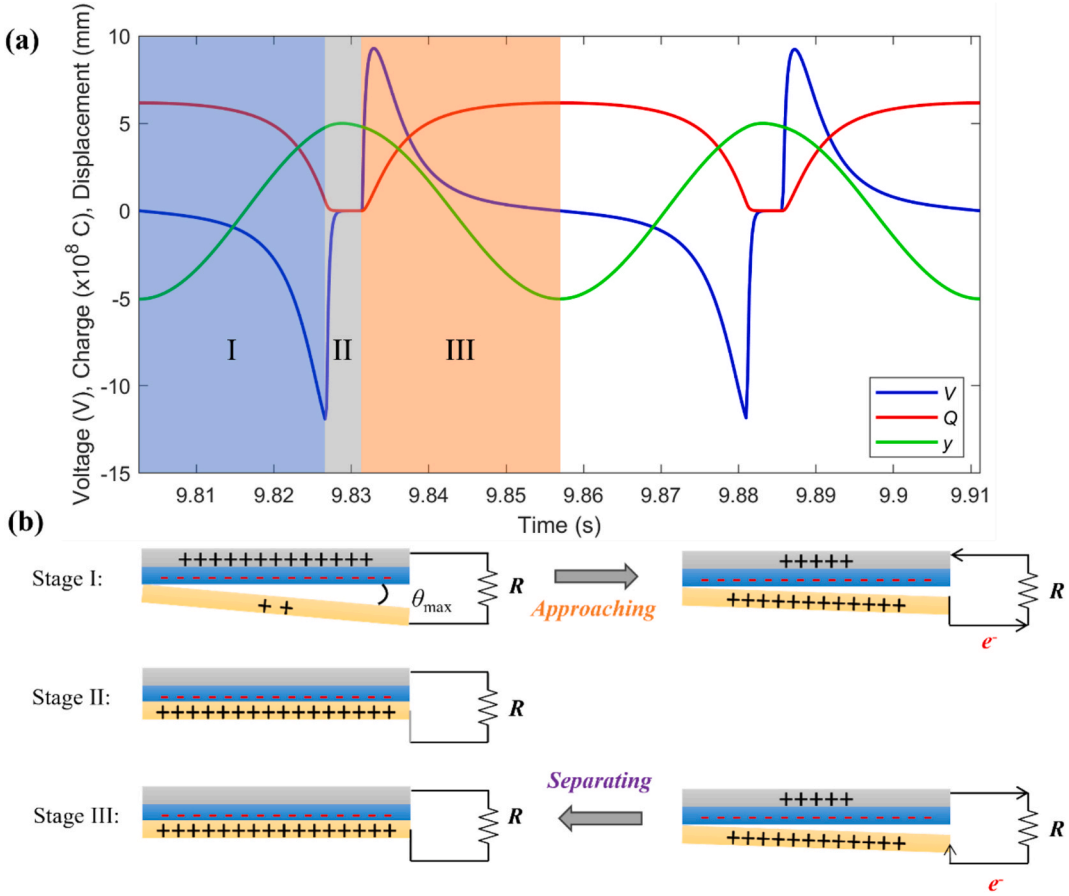


**Fig. 12.** (a) *V-Q-y* relationship and (b) its corresponding power-generation stages.

In addition to examining the time-domain responses, this case study also validates the frequency-domain responses. Indeed, it is particularly crucial to investigate the voltage and displacement responses in the frequency domain of a TEH under various external resistances. This is because, in practical applications, understanding the operational frequency range of the TEH's electromechanical responses—specifically, the available electrical voltage and corresponding mechanical displacement—is of utmost importance. Therefore, validating the ECM's capability to predict such responses from the TEH is essential. Within the ECM framework, frequency sweeps are conducted by calculating and recording the RMS voltages and displacements from the corresponding time-domain responses across different frequencies. Moreover, the resistance R value in the model can be adjusted to explore its effects on the output responses. In the experimental setup, the frequency sweep can be directly initiated through the vibration controller governing the seismic shaker's vibration. Simultaneously, an adjustable resistance box is utilized as the external resistance, allowing for resistance values to be varied from 0 to 10,000,000 O.

Fig. 13 presents the frequency sweep results of the RMS voltage and displacement obtained from both experimental data and ECM simulations, with a step size of 0.1 Hz for the sweep. These results span various excitation accelerations, ranging from 0.2 g to 0.5 g in 0.1 g increments. A high degree of agreement is evident between the experimental and simulated outcomes. Notably, the ECM accurately predicts the TEH's operating bandwidth and the available RMS voltage, thus confirming its efficacy in predicting the TEH's operating frequency range, RMS voltage, and corresponding displacement in the frequency domain. Moreover, Fig. 14 displays surface plots depicting the experimental and simulated RMS voltage and displacement of the TEH across excitation frequency and external resistance, with excitation acceleration set at 0.4 g. The ECM's results closely align with the experimental findings, showcasing an increase in output voltage with rising external resistance, consistent with Eq. (7). However, it is noteworthy that both sets of results indicate minimal influence of external resistance on the displacement of the TEH's beam, suggesting that the shunt effect can be disregarded for TEH systems [25].

Furthermore, it is important to note that the simulated and experimental RMS voltages in Fig. 13 do not deviate as obviously from each other as the time-domain responses in Fig. 11. RMS voltage is a more meaningful metric, as it better reflects the actual available DC voltage, which is directly related to the output power. Focusing on RMS voltage provides a more accurate representation of the energy harvester's performance and practical utility, especially in applications where consistent power delivery is critical.

While the peak-to-peak voltage discrepancies in Fig. 11 highlight the challenges of modeling nonlinear effects near resonance, the overall agreement for smaller excitations, where realistic ambient vibrations occur, remains substantial. Additionally, the consistency

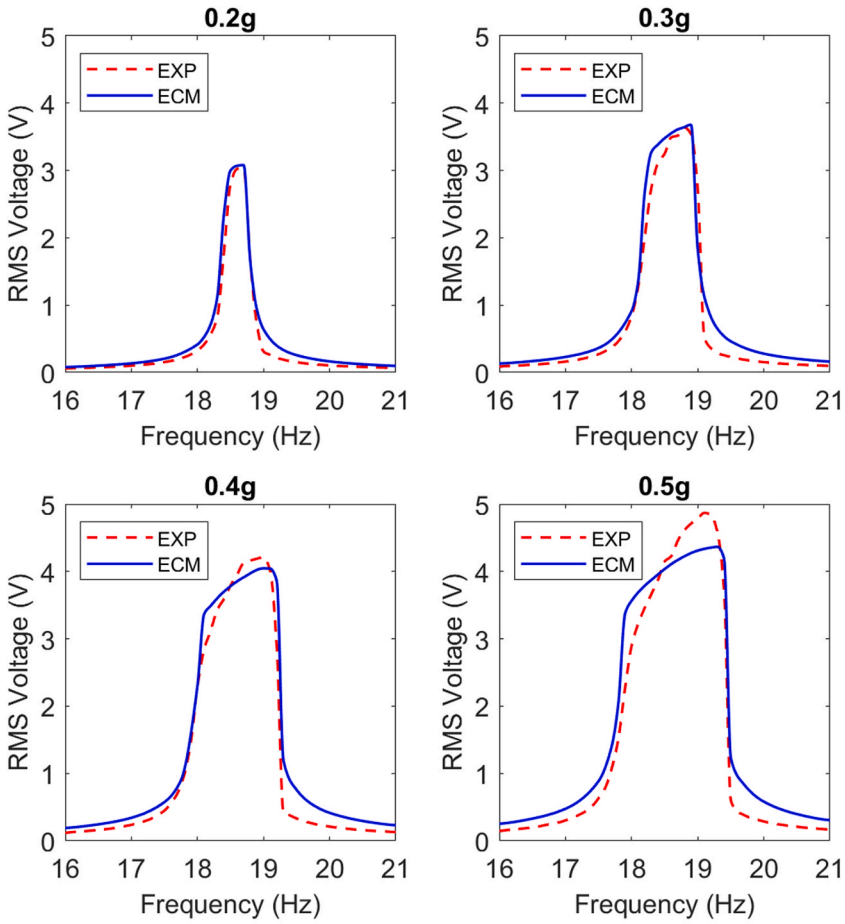


**(a)**

**Fig. 13.** Frequency-domain RMS (a) voltage response and (b) displacement response under various base excitations.

in the predictions of transferred charge and displacement is still respectable, even under higher excitation conditions. The alignment in RMS voltage further underscores that the equivalent circuit model remains a reliable tool for understanding and predicting the system's behavior.

Despite the remarkable agreements observed between the ECM and experimental results, certain disparities persist. Notably, discrepancies manifest in the rate of increase in the RMS voltage within the TEH's operating bandwidth, particularly where the RMS voltage tends to exhibit a linear rise in proximity to the TEH's natural frequency. Within this frequency band, it is assumed that the TEH's Cu electrode maintains complete contact with the PTFE film, with the voltage magnitude solely reliant on the available kinetic energy from the beam's vibration. However, experimental results indicate a steeper slope of increase in the RMS voltage within this frequency band. This phenomenon can be attributed to the imperfect contact between the triboelectric materials, where the voltage magnitude depends on both the completeness of contact and the available kinetic energy from the beam's vibration. The combined influence of these factors results in a more substantial increase in the RMS voltage within this linearly increasing domain in the experimental results. Furthermore, the agreement between experiment and simulation tends to decrease as excitation levels increase. This is attributed to heightened non-idealities in the experiment stemming from more significant vibro-impact, which proves challenging for the ECM to accurately encapsulate.

### *5.2. Experimental case study 2*

The previous case study successfully validated the electromechanical responses of the ECM, employing a simplified resistive circuit. In contrast, the second experimental case study aims to assess the ECM's efficacy in predicting the TEH's electrical response when connected to a more practical EEC (P-EEC). Instead of a simple resistor, the P-EEC utilized in this study comprises a bridge rectifier, a resistor, and a filter capacitor serving as an energy storage component. As depicted in Fig. 15 (a), the simplified circuit diagram of the

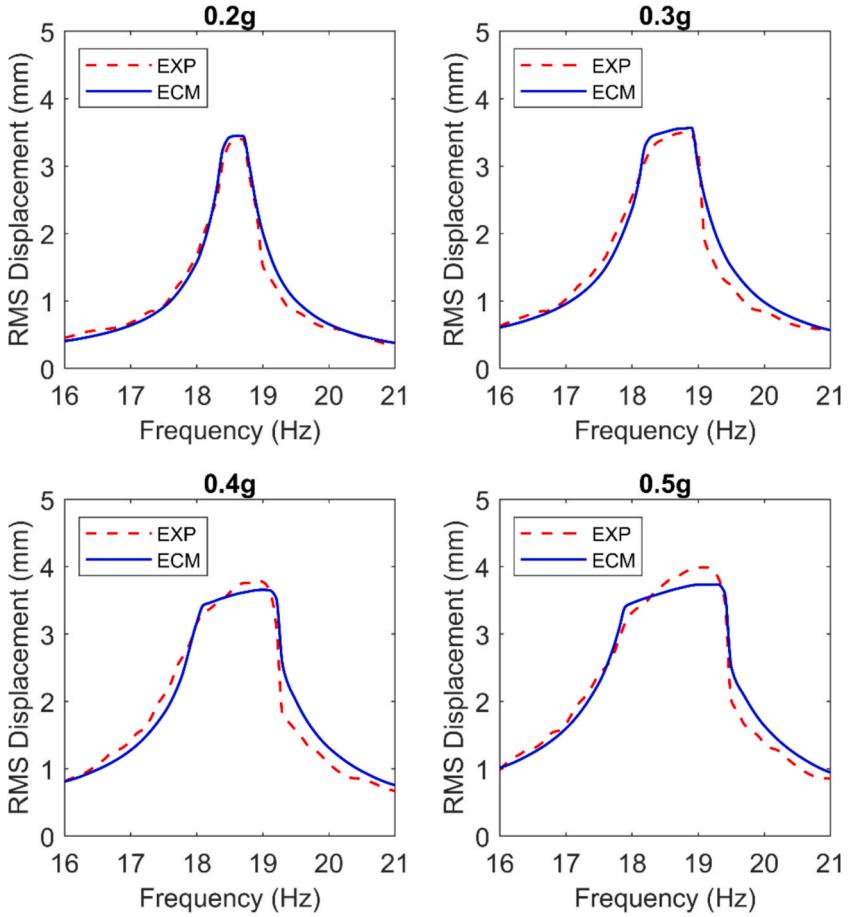


**(b)**

**Fig. 13.** (*continued*).

ECM features the replacement of the resistor $R$ in Fig. 7 with the P-EEC. The rectifier of the P-EEC is connected to the resistor $R$ via its DC output ports, with the filter capacitor $C_f$ operating in parallel. $C_f$ serves to smooth the pulsed FWR DC voltage generated by the TEH and stored by the rectifier, which also functions as the energy storage device. Upon reaching full charge, the accumulated voltage represents the equivalent DC voltage available from the TEH at the specified external resistance $R$. Fig. 15(b) illustrates the actual circuit implemented in the experiment, wherein a resistor box and a capacitor box are employed for $R$ and $C_f$, respectively. This setup represents a typical P-EEC in the experimental study.

In numerous studies, it has been demonstrated that an impedance mismatch exists between TEHs and energy-storing units [17,24], necessitating the determination of the optimal external resistance for maximizing power output from TEHs [24]. Unfortunately, existing literature lacks a model capable of predicting the optimal external resistance for TEH systems. However, by integrating the EEC model with the ECM model for TEHs on a system level, this study enables the prediction of the optimal resistance for TEHs. Experimental validation of this capability is conducted as follows. Initially, TEHs with identical parameters to those used in the previous section are employed. The base vibration operates at 18.4 Hz, with excitation accelerations ranging from 0.2 g to 0.5 g in linear increments of 0.1 g. Subsequently, the resistor $R$ is varied for each base excitation, ranging from 1 MΩ to 110 MΩ. At each $R$, the maximum accumulated voltage $V_{max}$ on $C_f$ is recorded and utilized to calculate the output power from the TEH according to

$$P = \frac{V_{\max}^2}{R} \tag{34}$$

As an illustration, Fig. 16 displays both the experimentally recorded and ECM simulated charging curves of a $C_f = 600$ nF filter capacitor with an external resistance $R = 6$ MΩ. With $V_{max} = 11$ V in this instance, the calculated power output is $P = 20.17$ μW.

The experimental and simulation results of available power against external resistance with varying excitations are depicted in Fig. 17 (a). It is evident that the ECM accurately predicts not only the optimal external resistance, occurring around 80 MΩ for the TEH,

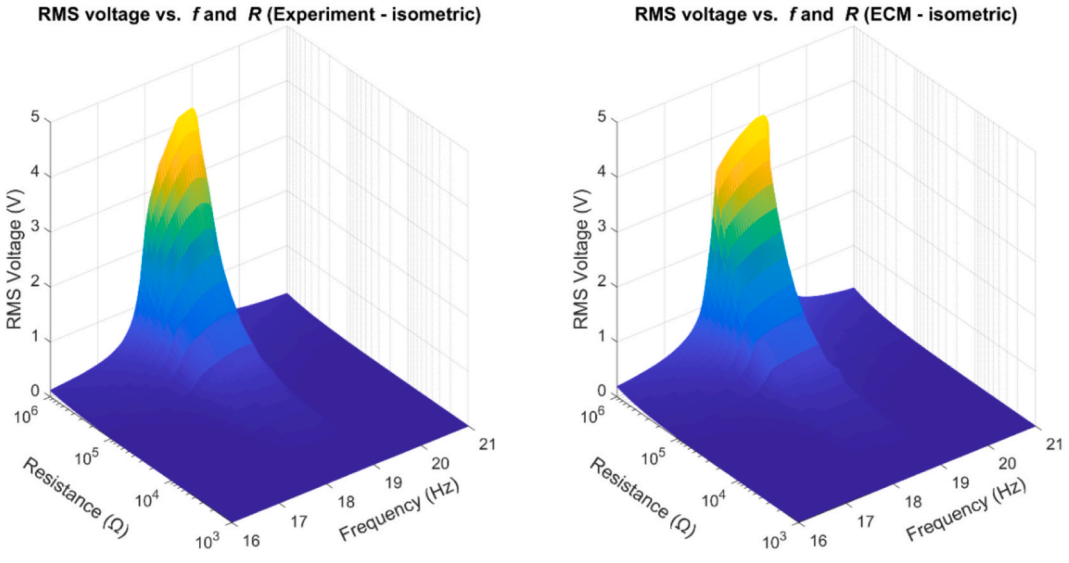


(a)

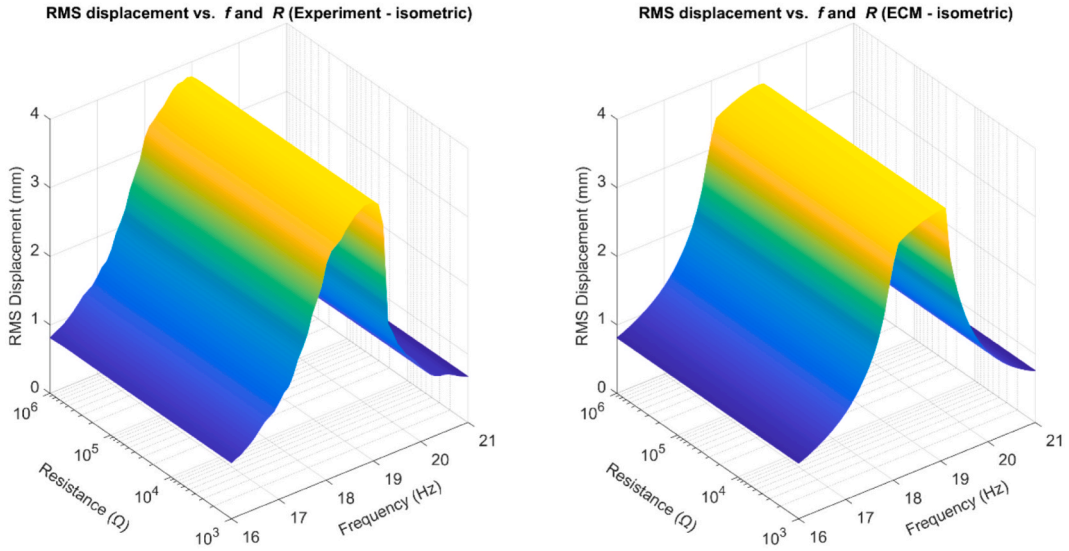


(b)

**Fig. 14.** (a) RMS voltage response and (b) RMS displacement response across excitation frequency and external resistance at 0.4 g base excitation.

but also the output power available from the TEH. Furthermore, it reveals that the effect of excitation acceleration on the optimal external resistance is negligible. Additionally, the effects of vibration frequency on output power are investigated. With the excitation fixed at 0.4 g, a frequency sweep is conducted at each resistance value, and the power at each frequency is calculated accordingly. The isometric and front views of the surface plot of power against both frequency and resistance are displayed in Fig. 17 (b) and (c), respectively. Consequently, the ECM effectively predicts the available power within the operating frequency range. These results demonstrate that the proposed ECM can be employed to identify the optimal external resistance without necessitating experimental trials. Furthermore, it is noteworthy that the optimal external resistance for TEHs is typically much higher than that for PEHs, as evidenced by the considerably higher optimal connected external resistance load for TEHs [44,45]. Through parametric studies, the ECM holds the potential to explore the parameters influencing the high internal impedance of TEHs, which often limits their current output to the microampere scale [18]. By identifying these influential parameters, it becomes feasible to devise methods aimed at

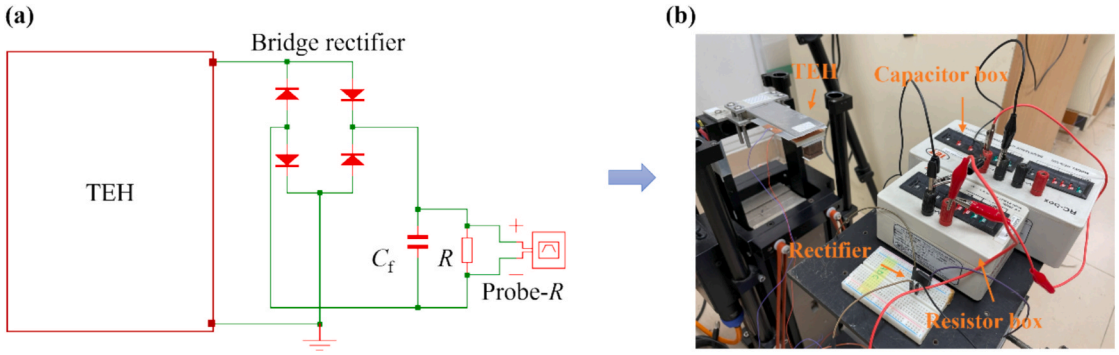


**Fig. 15.** (a) Simplified schematic diagram of ECM with a practical EEC connected; (b) physical prototype of the circuit implemented in the experiment.

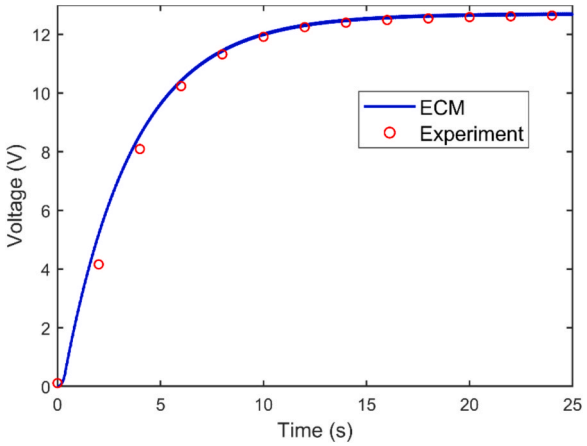


**Fig. 16.** Capacitor charging curve for a 600 nF capacitor with an external resistance of 6 MΩ.

reducing the internal impedance of TEHs, thereby enhancing their current output capabilities.

In addition to predicting the optimal external resistance, the ECM also captures the influence of excitation frequency on impedance matching behavior. As shown in Fig. 17 (b) and Fig. 17 (c), the optimal resistance remains relatively stable across the operating frequency range. This weak dependence on frequency simplifies the design of matching circuits and enhances the robustness of TEH systems in practical applications. In contrast, the available output power varies significantly with frequency, which is a critical consideration for real-world scenarios where ambient vibration frequencies may fluctuate unpredictably due to changing environmental or operational conditions. The ECM's ability to simulate such frequency-dependent behavior makes it a valuable tool for optimizing TEH performance under non-ideal and variable excitation conditions.

In numerous IoT applications, energy harvesters are tasked with charging the energy storage units of IoT sensors to specific voltage thresholds, triggering the sensors' operations [46]. Consequently, it is imperative for the ECM to accurately predict the accumulated voltage on $C_f$ during TEH operation. Hence, a series of capacitor-charging experiments and simulations are conducted to assess whether the proposed ECM can effectively predict real-time capacitor voltage during charging. Initially, the TEH is subjected to a 30-second base vibration at 18.4 Hz with an excitation acceleration of 0.4 g, while $C_f$ remains fixed at 600 nF and external resistances range from2 MΩ to 10 MΩ in 2 MΩ increments. The results with varying external resistance are depicted in Fig. 18 (a). Subsequently, resistance is held constant while excitation acceleration ranges from 0.2 g to 0.5 g, with the corresponding outcomes shown in Fig. 18 (b). Following this, resistance and excitation are fixed, while capacitance varies from 200 nF to 1000 nF in 200 nF increments, as shown in Fig. 18 (c). Finally, excitation frequency ranges from 1 Hz to 18.6 Hz with external resistance, filtering capacitance, and excitation held constant, and the results are displayed in Fig. 18 (d). In ECM simulations, Probe-$R$ is utilized to collect capacitor charging data, while experimental data is collected using an oscilloscope. A close alignment between experimental and ECM results is observed. However, due to the inevitable imperfections in real capacitors, such as parasitic capacitance or resistance, the rates of change of the charging curves in experimental and ECM results may vary slightly. Nonetheless, the final DC voltage values tend to converge because the predicted available power outputs by the ECM closely approximate the experimental results.

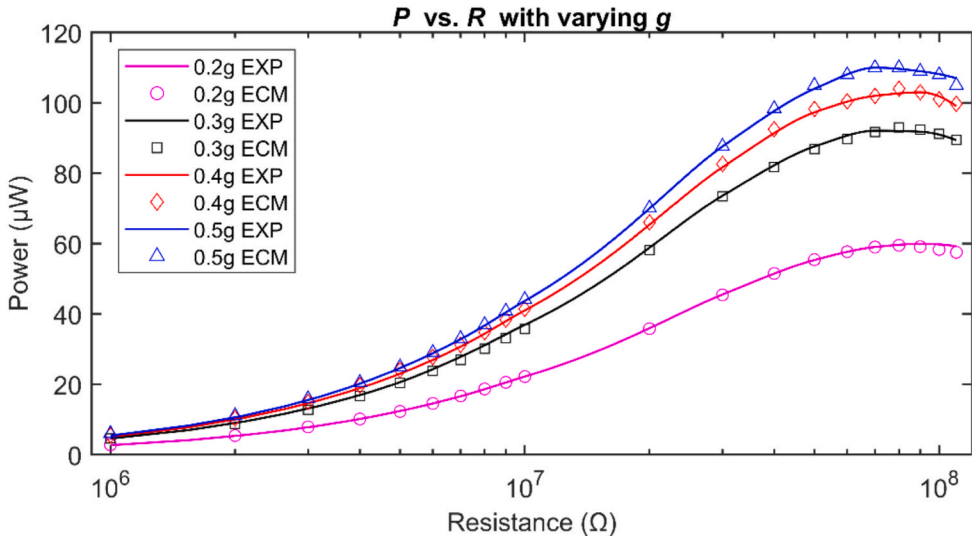


(a)

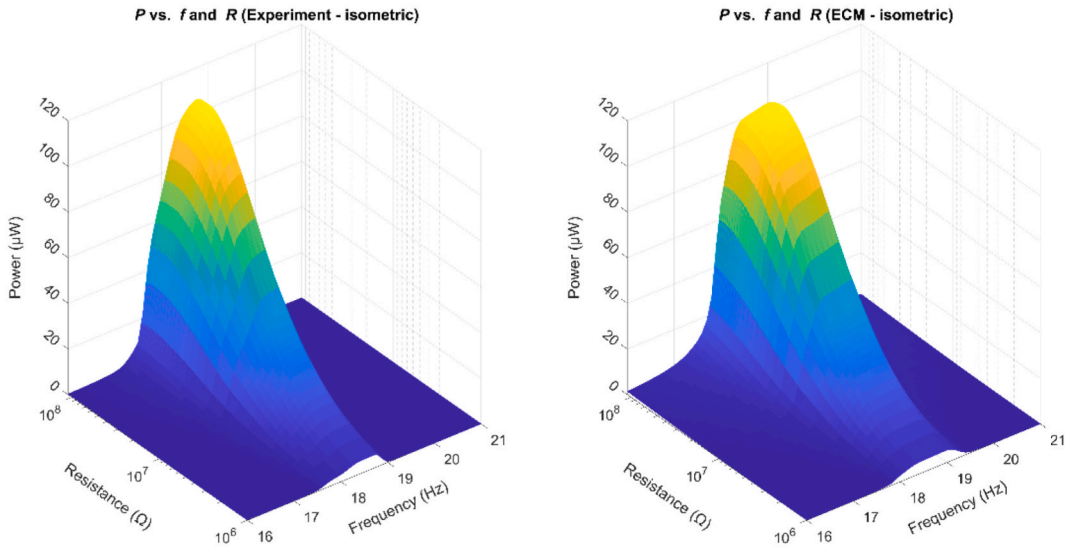


(b)

**Fig. 17.** Impedance-matching results from experiments and ECM simulations for TEH at base excitations ranging from 0.2 g to 0.5 g.

## 6. Conclusion

This paper introduces an equivalent circuit model (ECM) for a triboelectric energy harvester (TEH) operating in the contact-separation mode (CS mode) and validates its effectiveness through a comprehensive series of experimental case studies. Initially, a concise overview of the theoretical framework supporting the TEH's electromechanical model is presented. Subsequently, the ECM's parameters are determined from the governing equations, facilitating its establishment. Two experimental case studies are then conducted to validate the ECM's ability to forecast the TEH's electromechanical responses, followed by demonstrations of its capability to perform system-level simulations when connected to a practical energy extraction circuit (P-EEC). The experimental results closely align with the ECM's simulation results, affirming its efficacy as an alternative to conventional numerical simulations for TEHs, particularly for system-level simulations involving P-EECs. The study's main conclusions are summarized as follows:

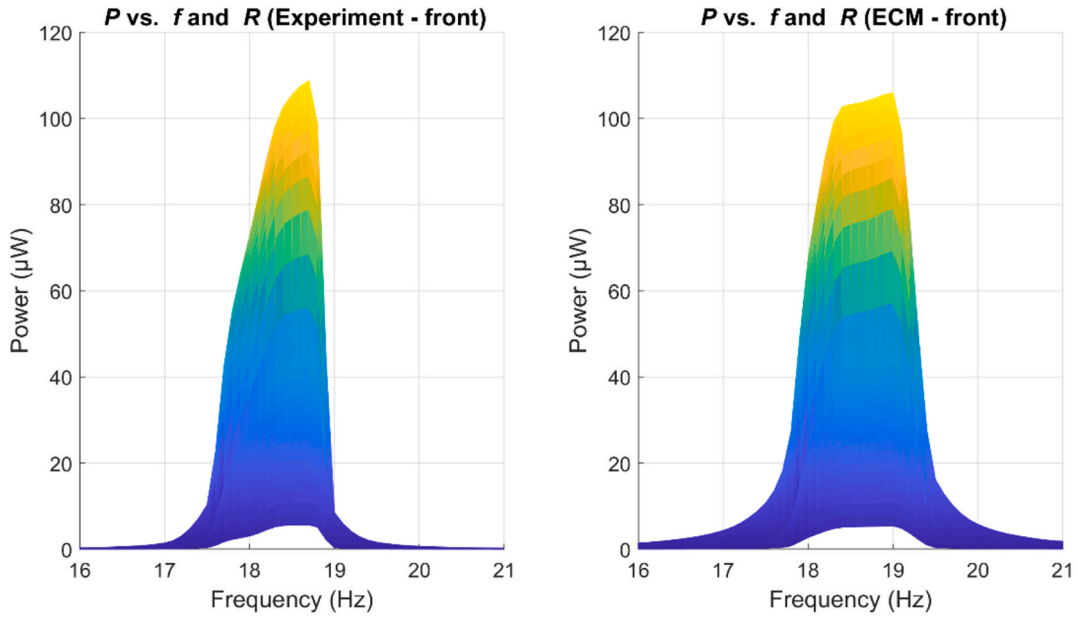


**(c)**

**Fig. 17.** (*continued*).

- **Innovative Modeling Approach**: The paper proposes a novel modeling technique for TEH systems using the ECM method, enabling system-level simulations for the first time in the field of triboelectric energy harvesting.
- **Parameter Identification**: Equivalent circuit parameters for the TEH's electromechanical model are identified by drawing analogies between circuitry and mechanical governing equations, such as the analogy between the governing equations of the forced RLC circuit and the forced damped vibration.
- **Handling Nonlinearity**: Nonlinear terms in the TEH's electromechanical model are represented using programmable transfer functions that act as arbitrary voltage sources in the circuit simulator. A pseudo-capacitor is innovatively incorporated to mathematically represent the back-and-forth coupling of the TEH's electromechanical model.
- **Experimental Validation**: An experimental case study is conducted to validate the ECM's ability to predict the TEH's electromechanical responses in both the time and frequency domains, including the *V-Q-x* relationship and the RMS voltage and displacement responses in the frequency and resistance domain.
- **System-Level Simulation**: Another experimental case study demonstrates the ECM's capability in system-level simulation. A rectified EEC comprising a resistor and a filter capacitor is employed, showcasing the ECM's competence in predicting optimal external resistance for maximum power generation and tracking voltage accumulation on the capacitor over time. This empowers the ECM for power analysis in TEHs, a task often challenging for numerical simulations based on analytical models.

In summary, this study highlights the potential and effectiveness of the ECM as a robust alternative for simulating TEH behavior, particularly in conducting system-level simulations involving practical EECs. The ECM enhances the understanding of TEH performance and provides valuable insights for optimizing these energy harvesters in real-world applications. In future work, the ECM can be extended to simulate and optimize the electromechanical responses of more complex TEHs, such as those with multi-degree-of-freedom supporting structures or hybrid TEHs that incorporate other transduction mechanisms, including but not limited to piezoelectric and electromagnetic transductions. Additionally, system-level simulations involving advanced P-EECs, such as synchronized switch harvesting on inductor circuits and synchronized charge extraction circuits, can also be achieved with the ECM, enabling more precise TEH system optimizations.

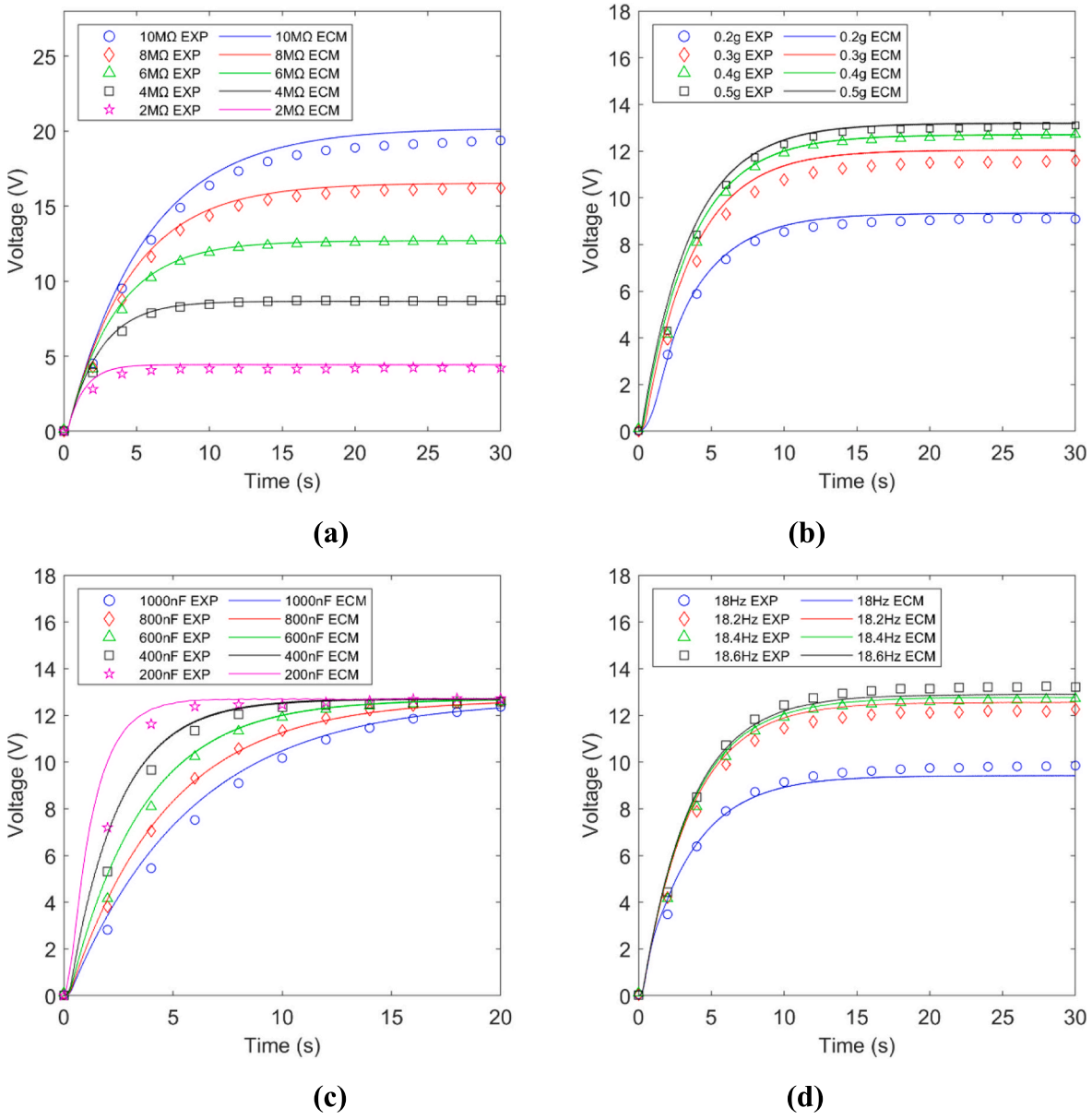


**Fig. 18.** Capacitor charging curves for (a) various external resistance values under 0.4 g excitation, 18.4 Hz frequency, and 600 nF filtering capacitance; (b) various excitation values under 6 MΩ external resistance, 18.4 Hz frequency, and 600 nF filtering capacitance; (c) various filtering capacitance values under 6 MΩ external resistance, 18.4 Hz frequency, and 0.4 g excitation; and (d) various frequency values under 6 MΩ external resistance, 600 nF filtering capacitance, and 0.4 g excitation.

## CRediT authorship contribution statement

**Zicheng Liu:** Writing – review & editing, Writing – original draft, Visualization, Validation, Software, Resources, Methodology, Formal analysis, Data curation, Conceptualization. **Guobiao Hu:** Writing – review & editing, Software, Resources, Investigation. **Xin Li:** Software, Resources, Investigation. **Chaoyang Zhao:** Writing – review & editing, Resources, Investigation. **Yaowen Yang:** Writing – review & editing, Supervision, Resources, Project administration, Investigation.

## Declaration of competing interest

The authors declare that they have no known competing financial interests or personal relationships that could have appeared to influence the work reported in this paper.

## Data availability

Data will be made available on request.

## References


[1] K.T. Prajwal, K. Manickavasagam, R. Suresh, A review on vibration energy harvesting technologies: analysis and technologies, Eur. Phys. J. Spec. Top. 231 (8) (2022/07/01 2022,) 1359–1371, https://doi.org/10.1140/epjs/s11734-022-00490-0.

[2] N. Sezer, M. Koç, A comprehensive review on the state-of-the-art of piezoelectric energy harvesting, Nano Energy 80 (2021/02/01/ 2021,) 105567, https://doi.org/10.1016/j.nanoen.2020.105567.

[3] S. Zhou, J. Cao, W. Wang, S. Liu, J. Lin, Modeling and experimental verification of doubly nonlinear magnet-coupled piezoelectric energy harvesting from ambient vibration, Smart Mater. Struct. 24 (5) (2015) 055008.

[4] Y. Tan, Y. Dong, X. Wang, Review of MEMS Electromagnetic Vibration Energy Harvester, J. Microelectromech. Syst. 26 (1) (2017) 1–16, https://doi.org/10.1109/JMEMS.2016.2611677.

[5] G. Miao, S. Fang, S. Wang, S. Zhou, A low-frequency rotational electromagnetic energy harvester using a magnetic plucking mechanism, Appl. Energy 305 (2022) 117838.

[6] F.U. Khan, M.U. Qadir, State-of-the-art in vibration-based electrostatic energy harvesting, J. Micromech. Microeng. 26 (10) (2016/09/20 2016,) 103001, https://doi.org/10.1088/0960-1317/26/10/103001.

[7] Z. Lai, et al., A hybrid piezo-dielectric wind energy harvester for high-performance vortex-induced vibration energy harvesting, Mech. Syst. Sig. Process. 150 (2021) 107212.

[8] Z. Lai, et al., Energy harvesting from a hybrid piezo-dielectric vibration energy harvester with a self-priming circuit, Energy 273 (2023) 127205.

[9] D.A. Barkas, C.S. Psomopoulos, P. Papageorgas, K. Kalkanis, D. Piromalis, A. Mouratidis, Sustainable Energy Harvesting through Triboelectric Nano – Generators: A Review of current status and applications, Energy Procedia 157 (2019/01/01/ 2019,) 999–1010, https://doi.org/10.1016/j.egypro.2018.11.267.

[10] Z. Li, Z. Saadatnia, Z. Yang, H. Naguib, A hybrid piezoelectric-triboelectric generator for low-frequency and broad-bandwidth energy harvesting, Energ. Conver. Manage. 174 (2018) 188–197.

[11] W. Tang et al., "Liquid-Metal Electrode for High-Performance Triboelectric Nanogenerator at an Instantaneous Energy Conversion Efficiency of 70.6%," Advanced Functional Materials, doi: 10.1002/adfm.201501331 vol. 25, no. 24, pp. 3718-3725, 2015/06/01 2015, doi: 10.1002/adfm.201501331.

[12] Y. Xie et al., "Grating-Structured Freestanding Triboelectric-Layer Nanogenerator for Harvesting Mechanical Energy at 85% Total Conversion Efficiency," Advanced Materials, doi: 10.1002/adma.201402428 vol. 26, no. 38, pp. 6599-6607, 2014/10/01 2014, doi: 10.1002/adma.201402428.

[13] Q. Shi, T. He, C. Lee, More than energy harvesting – Combining triboelectric nanogenerator and flexible electronics technology for enabling novel micro-/nano-systems, Nano Energy 57 (2019/03/01/ 2019,) 851–871, https://doi.org/10.1016/j.nanoen.2019.01.002.

[14] Y. Fu, H. Ouyang, R. Benjamin Davis, Nonlinear structural dynamics of a new sliding-mode triboelectric energy harvester with multistability, Nonlinear Dyn. 100 (3) (2020) 1941–1962.

[15] F.-R. Fan, Z.-Q. Tian, Z. Lin Wang, Flexible triboelectric generator, Nano Energy 1 (2) (2012/03/01/ 2012,) 328–334, https://doi.org/10.1016/j.nanoen.2012.01.004.

[16] Y. Peng, et al., Toward Highly Sensitive Ocean-Wave Monitoring With Sliding-Triboelectric Effect: Modeling, Experimental Validation, and Demonstration, IEEE/ASME Trans. Mechatron. (2024).

[17] L. Zhou, D. Liu, J. Wang, Z.L. Wang, Triboelectric nanogenerators: fundamental physics and potential applications, Friction 8 (3) (2020) 481–506.

[18] S. Niu, Z.L. Wang, Theoretical systems of triboelectric nanogenerators, Nano Energy 14 (2015) 161–192.

[19] S. Niu, et al., Theoretical study of contact-mode triboelectric nanogenerators as an effective power source, Energ. Environ. Sci. 6 (12) (2013) 3576–3583.

[20] S. Niu et al., "Theory of Sliding-Mode Triboelectric Nanogenerators," Advanced Materials, doi: 10.1002/adma.201302808 vol. 25, no. 43, pp. 6184-6193, 2013/11/01 2013, doi: 10.1002/adma.201302808.

[21] S. Niu, et al., Theory of freestanding triboelectric-layer-based nanogenerators, Nano Energy 12 (2015) 760–774.

[22] S. Niu et al., "Theoretical Investigation and Structural Optimization of Single-Electrode Triboelectric Nanogenerators," Advanced Functional Materials, doi: 10.1002/adfm.201303799 vol. 24, no. 22, pp. 3332-3340, 2014/06/01 2014, doi: 10.1002/adfm.201303799.

[23] J. Chen, et al., Harmonic-Resonator-Based Triboelectric Nanogenerator as a Sustainable Power Source and a Self-Powered Active Vibration Sensor, Adv. Mater. 25 (42) (2013) 6094–6099, https://doi.org/10.1002/adma.201302397.

[24] C. Zhao, G. Hu, Y. Yang, A cantilever-type vibro-impact triboelectric energy harvester for wind energy harvesting, Mech. Syst. Sig. Process. 177 (2022) 109185.

[25] Y. Fu, H. Ouyang, R.B. Davis, Nonlinear dynamics and triboelectric energy harvesting from a three-degree-of-freedom vibro-impact oscillator, Nonlinear Dyn. 92 (4) (2018/06/01 2018,) 1985–2004, https://doi.org/10.1007/s11071-018-4176-3.

[26] C. Zhao, Y. Yang, D. Upadrashta, L. Zhao, Design, modeling and experimental validation of a low-frequency cantilever triboelectric energy harvester, Energy 214 (2021) 118885.

[27] Y. Fu, H. Ouyang, R.B. Davis, Triboelectric energy harvesting from the vibro-impact of three cantilevered beams, Mech. Syst. Sig. Process. 121 (2019) 509–531.

[28] M. Pathak, R. Kumar, Modeling and analysis of energy extraction circuits for triboelectric nanogenerator based vibrational energy harvesting (SPIE Commercial + Scientific Sensing and Imaging), SPIE, 2018.

[29] M. Pathak, R. Kumar, Synchronous inductor switched energy extraction circuits for triboelectric nanogenerator, IEEE Access 9 (2021) 76938–76954.

[30] M. Pathak, R. Kumar, Self-propelled Pre-biased Synchronous Charge Extraction Circuit for Triboelectric Nanogenerator, IEEE Journal of Emerging and Selected Topics in Power Electronics 11 (1) (2022) 615–626.

[31] M. Pathak, R. Kumar, Synchronous pre-biasing of triboelectric nanogenerator for enhanced energy extraction, IEEE Trans. Power Electron. 37 (10) (2022) 11552–11566.

[32] W. Shunli et al., "Chapter 2 - Electrical equivalent circuit modeling," in Battery System Modeling, W. Shunli et al. Eds.: Elsevier, 2021, pp. 47-94.

[33] N.G. Elvin, A.A. Elvin, A General Equivalent Circuit Model for Piezoelectric Generators, J. Intell. Mater. Syst. Struct. 20 (1) (2009) 3–9, https://doi.org/10.1177/1045389x08089957.

[34] Y. Yang, L. Tang, Equivalent Circuit Modeling of Piezoelectric Energy Harvesters, J. Intell. Mater. Syst. Struct. 20 (18) (2009) 2223–2235, https://doi.org/10.1177/1045389x09351757.

[35] L. Zhao, L. Tang, Y. Yang, Synchronized charge extraction in galloping piezoelectric energy harvesting, J. Intell. Mater. Syst. Struct. 27 (4) (2016) 453–468, https://doi.org/10.1177/1045389x15571384.

[36] J. Jia, X. Shan, X. Zhang, T. Xie, Y. Yang, Equivalent circuit modeling and analysis of aerodynamic vortex-induced piezoelectric energy harvesting, Smart Mater. Struct. 31 (3) (2022) 035009.

[37] B. Bayik, A. Aghakhani, I. Basdogan, A. Erturk, Equivalent circuit modeling of a piezo-patch energy harvester on a thin plate with AC–DC conversion, Smart Mater. Struct. 25 (5) (Apr 2016) 055015, https://doi.org/10.1088/0964-1726/25/5/055015.

[38] H. Zhao, H. Ouyang, A capsule-structured triboelectric energy harvester with stick-slip vibration and vibro-impact, Energy 235 (2021/11/15/ 2021,) 121393, https://doi.org/10.1016/j.energy.2021.121393.

[39] Q. Zhu, G. Wang, Y. Zheng, Z. Liu, S. Zhou, B. Zhang, Coupling nonlinearities and dynamics between the hybrid tri-stable piezoelectric energy harvester and nonlinear interfaced circuit, Appl. Energy 323 (2022) 119636.

[40] C.J. Rupp, M.L. Dunn, K. Maute, Analysis of piezoelectric energy harvesting systems with non-linear circuits using the harmonic balance method, J. Intell. Mater. Syst. Struct. 21 (14) (2010) 1383–1396.

[41] C. Zhao, G. Hu, X. Li, Z. Liu, W. Yuan, Y. Yang, Wide-bandwidth triboelectric energy harvester combining impact nonlinearity and multi-resonance method, Appl. Energy 348 (2023) 121530.
[42] J. Henniker, "Triboelectricity in Polymers," Nature, vol. 196, no. 4853, pp. 474-474, 1962/11/01 1962, doi: 10.1038/196474a0.
[43] Z. Liu, C. Zhao, G. Hu, Y. Yang, A multi-degree-of-freedom triboelectric energy harvester for dual-frequency vibration energy harvesting, Mech. Syst. Sig. Process. 188 (2023) 109951.
[44] A. Sharma, P. Agarwal, Experimental study of resistive load for impedance matching of triboelectric energy harvester fabricated with patterned polydimethylsiloxane polymer layer, SN Appl. Sci. 2 (6) (2020) 1058.
[45] K. Yang, C. Zheng Jun, D. John, S. Jim, Z. Meiling, Strongly coupled piezoelectric energy harvesters: Optimised design with over 100 mW power, high durability and robustness for self-powered condition monitoring, Energ. Conver. Manage. 237 (2021) 114129, https://doi.org/10.1016/j.enconman.2021.114129.
[46] G. Hu, C. Zhao, Y. Yang, X. Li, J. Liang, Triboelectric energy harvesting using an origami-inspired structure, Appl. Energy 306 (2022) 118037.